Published OnlineFirst November 7, 2014; DOI: 10.1158/0008-5472.CAN-13-2037

Therapeutics, Targets, and Chemical Biology

Cancer Research

VEGF-Targeted Therapy Stably Modulates the Glycolytic Phenotype of Tumor Cells

Matteo Curtarello[1], Elisabetta Zulato[1], Giorgia Nardo[1], Silvia Valtorta[2,3], Giulia Guzzo[4], Elisabetta Rossi[5], Giovanni Esposito[1], Aichi Msaki[1], Anna Pastò[1], Andrea Rasola[4], Luca Persano[6], Francesco Ciccarese[1], Roberta Bertorelle[1], Sergio Todde[2], Mario Plebani[7], Henrike Schroer[8], Stefan Walenta[8], Wolfgang Mueller-Klieser[8], Alberto Amadori[1,5], Rosa Maria Moresco[2,3], and Stefano Indraccolo[1]

Abstract

Anti-VEGF therapy perturbs tumor metabolism, severely impairing oxygen, glucose, and ATP levels. In this study, we investigated the effects of anti-VEGF therapy in multiple experimental tumor models that differ in their glycolytic phenotypes to gain insights into optimal modulation of the metabolic features of this therapy. Prolonged treatments induced vascular regression and necrosis in tumor xenograft models, with highly glycolytic tumors becoming treatment resistant more rapidly than poorly glycolytic tumors. By PET imaging, prolonged treatments yielded an increase in both hypoxic and proliferative regions of tumors. A selection for highly glycolytic cells was noted and this metabolic shift was stable and associated with increased tumor aggressiveness and resistance to VEGF blockade in serially transplanted mice. Our results support the hypothesis that the highly glycolytic phenotype of tumor cells studied in xenograft models, either primary or secondary, is a cell-autonomous trait conferring resistance to VEGF blockade. The finding that metabolic traits of tumors can be selected by antiangiogenic therapy suggests insights into the evolutionary dynamics of tumor metabolism. *Cancer Res; 75(1); 120–133. ©2014 AACR.*

Introduction

Among various angiogenic factors, VEGF plays a crucial role in tumor angiogenesis (1). Neutralization of the VEGF pathway impairs tumor growth and this notion has provided ground for development of antiangiogenic drugs (2). However, both preclinical models and clinical trials have shown that benefits from first-generation angiogenesis inhibitors are generally short-term, due to the development of intrinsic as well as acquired resistance (3, 4). Apart from vascular resistance, due to bypassing of VEGF blockade by proangiogenic factors produced by either tumor cells, stromal cells or various types of bone marrow-derived cells, resistance has also been associated with selection of clones resistant to hypoxia, acquisition of an invasive phenotype, and overexpression of c-Met (3, 5, 6).

Metabolism of tumors differs remarkably from that of the tissues of their origin. Tumor cells exhibit altered pathways of biomass and energy production that allow them to sustain higher proliferative rates and resist some cell death signals, such as those mediated by increased oxidative damage (7). To divide, cells need to both increase their size and replicate DNA, processes that are metabolically demanding and require large quantities of proteins, lipids and nucleotides, as well as energy in the form of ATP. Major metabolic alterations of cancer cells are the enhanced glucose uptake and glycolysis under aerobic conditions, increased glutamine utilization and *de novo* fatty acid synthesis (7) and the more recently characterized aberrant choline phospholipid metabolism (8). Metabolic alterations in cancer cells may derive from genetic changes associated with cell transformation such as dysregulated activity of HIF1 (9), loss of p53 or altered expression of *c-Myc* or *Akt* (10), or be triggered by inhibition of mitochondrial respiration (11). Moreover, changes in tumor metabolism can also follow reduction in energy sources (O_2, glucose, glutamine) in the tumor microenvironment associated with antiangiogenic therapy (12–14).

Although in patients anti-VEGF therapy is generally combined with chemotherapy, in preclinical studies its administration as monotherapy is a strategy to better discern downstream effects of antiangiogenic drugs from cytotoxic drugs. We recently reported that short-term anti-VEGF therapy causes severe impairment of glucose and ATP levels in tumors (14). In this study, we also found that the response to short-term

[1]Istituto Oncologico Veneto, IRCCS, Padova, Italy. [2]IBFM-CNR, Segrate, Italy; Tecnomed Foundation and Department of Health Sciences, University of Milan-Bicocca, Monza, Italy. [3]Experimental Imaging Center, IRCCS San Raffaele Scientific Institute, Milan, Italy. [4]Department of Biomedical Sciences, University of Padova, Padova, Italy. [5]Department of Surgery, Oncology and Gastroenterology, University of Padova, Padova, Italy. [6]Onco-hematology Laboratory, Department of Woman and Child Health, University of Padova, Padova, Italy. [7]Department of Laboratory Medicine, University-Hospital, Padova, Italy. [8]Institute of Physiology and Pathophysiology, University Medical Center of the Johannes Gutenberg University Mainz, Germany.

Note: Supplementary data for this article are available at Cancer Research Online (http://cancerres.aacrjournals.org/).

R.M. Moresco and S. Indraccolo contributed equally to this article.

Corresponding Author: Stefano Indraccolo, Istituto Oncologico Veneto, IRCCS, via Gattamelata, 64-35128 Padua, Italy. Phone: 3904-9821-5875; Fax: 3904-9807-2854; E-mail: stefano.indraccolo@unipd.it

doi: 10.1158/0008-5472.CAN-13-2037

Published OnlineFirst November 7, 2014; DOI: 10.1158/0008-5472.CAN-13-2037

VEGF blockade is strongly dependent on the glycolytic phenotype of the tumor. Specifically, highly glycolytic tumor xenografts developed large necrotic areas following short-course VEGF neutralization, whereas xenografts characterized by relatively low glycolytic activity remained substantially viable (14). To investigate whether metabolic features could affect the therapeutic outcome, here we analyzed long-term effects of anti-VEGF treatment on tumor xenografts characterized by different levels of glucose addiction. The results show that highly glycolytic tumors rapidly acquire resistance to VEGF neutralization. Moreover, based on results of metabolic assays in four different tumor models, we report for the first time that anti-VEGF therapy causes stable selection of highly glycolytic tumor cells, indicating that the metabolic phenotype of tumors can change following administration of antiangiogenic drugs.

Materials and Methods

Cell culture and treatments

Several tumor cell lines representative of highly glycolytic (OC316 and MCF7) or poorly glycolytic (IGROV-1 and SKOV3) cells were used in this study (Supplementary Fig. S1; ref. 14). IGROV-1 and MCF-7 cells were purchased from ATCC, OC316 cells were provided by S. Ferrini (IST, Genoa, Italy), SKOV3 cells was kindly provided by S. Canevari (INT, Milan, Italy). IGROV-1, OC316 and SKOV3 were grown in RPMI1640 (Euroclone) supplemented with 10% fetal calf serum (FCS; Life Technologies), 1% HEPES (10 mmol/L, Cambrex Bioscience), 1% L-glutamine (2mmol/L), 1% sodium pyruvate (1 mmol/L), and 1% antibiotic-antimycotic mix (Gibco-BRL). MCF-7 cells were grown in DMEM (Euroclone) supplemented with 10% FCS and 1% antibiotic-antimycotic mix. Cultures were maintained at 37°C in a humidified 5% CO_2/95% air atmosphere. Where specified, tumor cells were treated with 2-deoxyglucose (2-DG; Sigma-Aldrich) at 6 g/L for 72 hours before apoptosis evaluation. Hypoxic treatment (0.5% O_2) was achieved by incubating cells in an InVivo2 300 hypoxic chamber (Ruskinn Technology).

In vivo experiments

Procedures involving animals and their care conformed with institutional guidelines that comply with national and international laws and policies (EEC Council Directive 86/609, OJ L 358, 12 December, 1987). For tumor establishment, 8-week-old SCID mice (Charles River) were subcutaneously injected into both flanks with 0.3–0.5 $\times$ 10^6 tumor cells mixed at 4°C with liquid Matrigel (Becton Dickinson). Tumor volume (mm^3) was calculated as previously reported (15).

To generate the PDOVCA37 xenograft, following informed consent, ascitic fluid of one patient with ovarian cancer was obtained from the Medical Oncology Unit of our Institute. Tumor cells (2 $\times$ 10^6) were injected intraperitoneally into SCID mice, as reported elsewhere (16). About 2 months later, animals developed tumors that contained both a solid and an ascitic component. These tumors were serially passaged two times into SCID mice before transduction with a luciferase-encoding lentiviral vector. For optical imaging, bioluminescence signals were acquired on IVIS Imaging System (Xenogen Corporation) as described elsewhere (17).

In a set of experiments, 20-week-old female BALB-neuT mice bearing measurable mammary tumors (3 mm diameter) were used (18). Founder BALB-neuT male mice were kindly provided by Biogem following agreement with Dr. Guido Forni (University of Torino, Torino, Italy). BALB-neuT mice were bred in house with BALB/c female mice. Female offsprings were then screened for the presence of Her2/*neu* oncogene as previously described (19).

Anti-human VEGF monoclonal antibody (mAb; bevacizumab) or anti-human/mouse VEGF mAb (B20-4.1.1; ref. 20) were administered intraperitoneally at 100 μg/dose bi- or triweekly to SCID and BALB-neuT mice, respectively, and mice were sacrificed 48 hours after the last treatment. Control mice received intraperitoneal injections of PBS.

Reverse transcription PCR and real-time PCR assay

Total RNA was extracted using the RNeasy Mini Kit (Qiagen) according to the manufacturer's instructions. cDNA was synthesized from 0.5 to 1 μg of total RNA using the Superscript II reverse transcriptase (Invitrogen). Real-time PCR was performed with SYBR Green dye and Gene AMP 5700 Sequence Detection System (PE Biosystems). Cycling conditions were 10 minutes at 95°C, 40 cycles of 15 seconds at 95°C, and 1 minute at 60°C. Each sample was run in duplicate. For all genes evaluated, mRNA was normalized to β2-microglobulin (*B2M*) mRNA by subtracting the cycle threshold (C_t) value of *B2M* mRNA from the C_t value of the gene of interest (ΔC_t). Fold difference ($2^{-\Delta\Delta C_t}$) was calculated by subtracting the ΔC_t (treated sample) to ΔC_t (reference sample), to generate a $\Delta\Delta C_t$. PCR efficiency was in the range 95% to 105%. Primers used for real-time PCR are listed under Supplementary Table SI.

Glucose and lactate measurements

Glucose and lactate concentrations in supernatants were determined by colorimetric methods on an automated analyzer (Dimension RxL, Dade Behring). Values were normalized to cells number at the end of the incubation period.

Oxygen consumption rate and extracellular acidification rate analysis

Oxygen consumption rate (OCR) and extracellular acidification rate (ECAR) were assessed in real-time with a XF24 Extracellular Flux Analyzer (Seahorse Biosciences) as described (11). Briefly, cells (2.5 $\times$ 10^4/well) were plated in RPMI medium supplemented with 10% FBS. The next day, cells were placed in a running DMEM medium (supplemented with 25 mmol/L D-glucose, 2 mmol/L glutamine, 1 mmol/L sodium pyruvate, and without serum and bicarbonate) and preincubated for 30 minutes at 37°C in atmospheric CO_2 before starting metabolic measurements. At the end of the experiment, OCR and ECAR values were normalized for the protein content of each sample. Accurate titration with the uncoupler FCCP was performed for each cell type, to utilize the FCCP concentration (400 nmol/L) that maximally increases OCR without being toxic.

Positron emission tomography studies

Cell proliferation and regional tissue hypoxia were investigated using [^{18}F]-fluorothymidine (FLT) and [^{18}F]-

Published OnlineFirst November 7, 2014; DOI: 10.1158/0008-5472.CAN-13-2037

fluoroazomycin arabinoside (FAZA) as radioligands, respectively, and YAP-(S)-PET II (ISE, Pisa, Italy) small animal scanner (21, 22). Further details of PET studies are reported under Supplementary Data.

Induced metabolic bioluminescence imaging

Freeze-clamped tumors were excised and cut into serial cryosections for structural hematoxylin and eosin staining and metabolic measurements. For quantitative measurement of ATP, lactate and glucose, the method of metabolic imaging with induced bioluminescence (imBI) was applied, as described before (23–25). Further details of imBI are reported under Supplementary Data.

Statistical analysis

Results were expressed as mean value ± SD. Statistical comparison between two sets of data was performed using either the unpaired Student *t* test (two-tailed) or, in the case of analysis of glucose and lactate levels in supernatants, the Mann–Whitney test (two-tailed). To analyze PET data, ANOVA followed by the Bonferroni *post hoc* test for multiple comparisons was used. Differences were considered statistically significant at $P < 0.05$.

Further experimental details are available under Supplementary Data.

Results

The glycolytic phenotype of tumors modulates resistance to anti-VEGF therapy

Following establishment of tumor xenografts, mice were treated with two or three weekly administrations of the anti-VEGF antibody bevacizumab for 4 weeks. Results show marked growth arrest of poorly glycolytic IGROV-1 tumors, whereas highly glycolytic OC316 xenografts after an initial shrinkage became substantially resistant to antiangiogenic therapy according to measurements of tumor size, although at sacrifice of the mice tumors were still smaller compared with controls (Fig. 1). *Ad interim* histologic analysis performed in samples analyzed after 7 days of treatment showed higher levels of necrosis in highly glycolytic OC316 compared with poorly glycolytic IGROV-1 tumors (data not shown), in line with our previous observations (14). In contrast, analysis of tumor samples collected at day 28 disclosed abundant necrotic areas in all anti–VEGF-treated tumors (Supplementary Fig. S2A). Microvessel density was significantly lower in tumors treated with anti-VEGF at day 28 after treatment (Supplementary Fig. S2B), indicating that tumor angiogenesis was still partially dependent on VEGF at the end of treatment. These results were further validated by anti-VEGF treatment of additional tumor xenografts. MCF7 and SKOV3 represent other examples of relatively highly and poorly glycolytic tumor cell lines, respectively, as shown by glucose consumption and lactate

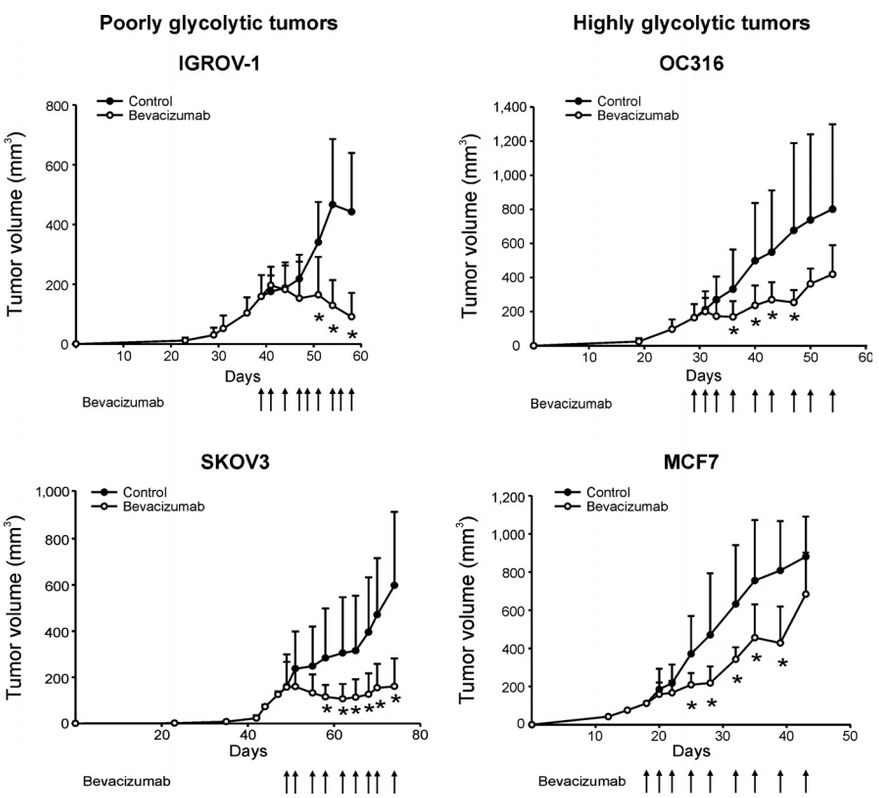

Figure 1.
Highly glycolytic tumors become rapidly resistant to anti-VEGF therapy. Kinetics of tumor development in SCID mice subcutaneously injected with poorly (left) and highly (right) glycolytic tumor cells and effects of multiple injections of the anti-VEGF mAb bevacizumab (arrows, 100 μg/dose administered bi- or triweekly) on tumor size compared with the size of controls ($n = 6$ mice for group). *, $P < 0.05$, *t* test. Tumors were collected and analyzed two days after the last dose of anti-VEGF mAb or PBS for bevacizumab and control groups, respectively.

production levels *in vitro* (Supplementary Fig. S1A) as well as sensitivity to glucose starvation/hypoxia and treatment with 2-DG (Supplementary Fig. S1B). Following anti-VEGF therapy, SKOV3 tumors were almost completely starved, whereas MCF7 xenografts became rapidly resistant (Fig. 1).

Since these results could also in part depend on the different genetic background of the various tumor cell lines, we sought to corroborate them by using pairs of isogenic cells with different metabolic profiles. To this end, we exploited tumor cells bearing reduced expression of both AMPKα1 and α2 subunits. Ground for this experiment was provided by our previous study, which indicated that *AMPK* silencing in IGROV-1 cells leads to acquisition of highly glycolytic features (14) as well as by a recent study that reported that AMPK is a negative regulator of aerobic glycolysis in tumor cells (26). As expected, double silencing of *AMPKα1* and *α2* by shRNA delivery was followed by reduced *AMPKα* RNA and protein levels in IGROV-1 cells (Supplementary Fig. S3A) and was associated with significantly increased levels of glucose consumption and lactate production *in vitro* (Supplementary Fig. S3B) and much higher cell death under glucose starvation or hypoxia compared to control cells (Supplementary Fig. S3C). Proliferation and viability of IGROV-1 shAMPKα1/α2 cells under standard culture conditions were similar to that of control cells (not shown). However, tumors formed by IGROV-1 shAMPKα1/α2 cells had somewhat accelerated growth compared with control tumors (Supplementary Fig. S3D). Following treatment with bevacizumab, tumors formed by IGROV-1 cells transduced by an irrelevant shRNA regressed similarly to parental IGROV-1 tumors; in contrast, tumors formed by IGROV-1 cells bearing attenuated AMPK α1/α2 levels initially regressed but subsequently became resistant to anti-VEGF therapy (Supplementary Fig. S3D). Altogether, these findings suggest a negative association of the glycolytic phenotype of tumor cells with therapeutic responses to VEGF blockade in SCID mice.

Selection of highly glycolytic tumor cells following VEGF blockade

Our previous study indicated that the amount of tumor necrosis following VEGF blockade in part depends on the glycolytic phenotype of tumor cells, being much lower in poorly glycolytic than in highly glycolytic xenografts (14). The observation of large necrotic areas in IGROV-1 tumors following long-term anti-VEGF therapy (Supplementary Fig. S2A) suggested that the low glycolytic phenotype of these tumor cells could be modulated by anti-VEGF therapy. To investigate this possibility, we stained tumor sections with anti-monocarboxylate transporter 4 (MCT4), a lactic acid transporter that clearly distinguishes OC316 from IGROV-1 cells *in vitro* (27). As shown in Fig. 2A, this glycolytic marker was expressed at much higher levels in OC316 than in IGROV-1 tumors. The latter had negligible MCT4 expression following short-term (7 days) anti-VEGF therapy whereas after prolonged anti-VEGF treatment (28 days) MCT4 expression increased compared to control tumors (Fig. 2A). Similar results were found in SKOV-3 tumors following antiangiogenic therapy, although in this case prominent up-regulation of MCT1 - another member of the MCT family - was observed (Fig. 2A). Importantly, marked MCT1 expression was also found in clinical liver metastasis samples of colorectal cancer treated with chemotherapy plus bevacizumab (Fig. 2A), suggesting that this phenomenon occurs also in patients treated with anti-VEGF drugs. In experimental tumors, HIF1α—a transcription factor that is strongly stabilized under hypoxic conditions and regulates expression of several glycolysis-associated transcripts, including MCT4 (28)—was found mainly expressed in the nuclei of tumor cells after anti-VEGF therapy compared with prevalently cytoplasmic expression in control samples (Fig. 2B). These data indicate a metabolic shift in tumors treated with anti-VEGF therapy and suggest that HIF1α-mediated up-regulation of glycolysis could in part account for increased expression of lactate transporters in tumors.

Anti–VEGF-treated tumors contain a highly proliferative and hypoxic core

Since metabolic reprogramming, hypoxia and cell proliferation are strictly intertwined (9), we next investigated the proliferative activity of tumors treated with anti-VEGF therapy. To this end, [^{18}F]FLT PET was exploited to functionally measure the dynamics of proliferation in IGROV-1 and OC316 xenografts. To evaluate the extension and distribution of cell phenotypes in tumors, we measured the volume of distribution of [^{18}F]FAZA, as a marker of hypoxic regions within tumors. In both xenografts, 7 days after anti-VEGF therapy, the volume of highly proliferative regions was similar to pretreatment values. At the end of therapy (day 28), in IGROV1 tumors, nevertheless a cytostatic effect in tumor volume measured at caliper, we found increased [^{18}F]FLT distribution compared with previous measurements (Fig. 3A), indicating that tumors treated with bevacizumab were composed by highly proliferative cells. This was also accompanied by a progressive increase of tumor hypoxic areas compared with pretreatment values, as shown by results of [^{18}F]FAZA PET (Fig. 3A). PET analysis disclosed similar changes in proliferation and hypoxic areas also in OC316 tumors, that acquired resistance to VEGF neutralization (Fig. 3B). We observed a significant difference in tumor volume measured at caliper between treated and control group at 28 days, although tumor size increased compared with baseline. In addition, a concomitant enlargement of highly proliferative and hypoxic areas was noted.

Proliferation was further studied in tumor sections by staining with antiphosphohistone3 (p-H3) antibody, an *in situ* marker of cell proliferation. Results showed significantly reduced numbers of p-H3^{+} cells in anti–VEGF-treated IGROV-1 at 7 days after treatment, whereas numbers comparable with control IGROV-1 were found at day 28 (Supplementary Fig. S4). Altogether, these results suggest that continuous VEGF blockade eventually selects for a population of cells with high proliferative activity embedded in an hypoxic microenvironment, which may account for the increased expression of glycolysis-associated markers observed.

VEGF blockade is associated with stable modulation of aerobic glycolysis in tumor cells

To better characterize metabolic changes observed after prolonged (28 days) anti-VEGF therapy in tumors, we set up *ex vivo* cultures of tumor cells. Measurement of glucose consumption and lactate production indicated that cultures from anti–VEGF-treated IGROV-1 tumors had slightly but

Published OnlineFirst November 7, 2014; DOI: 10.1158/0008-5472.CAN-13-2037

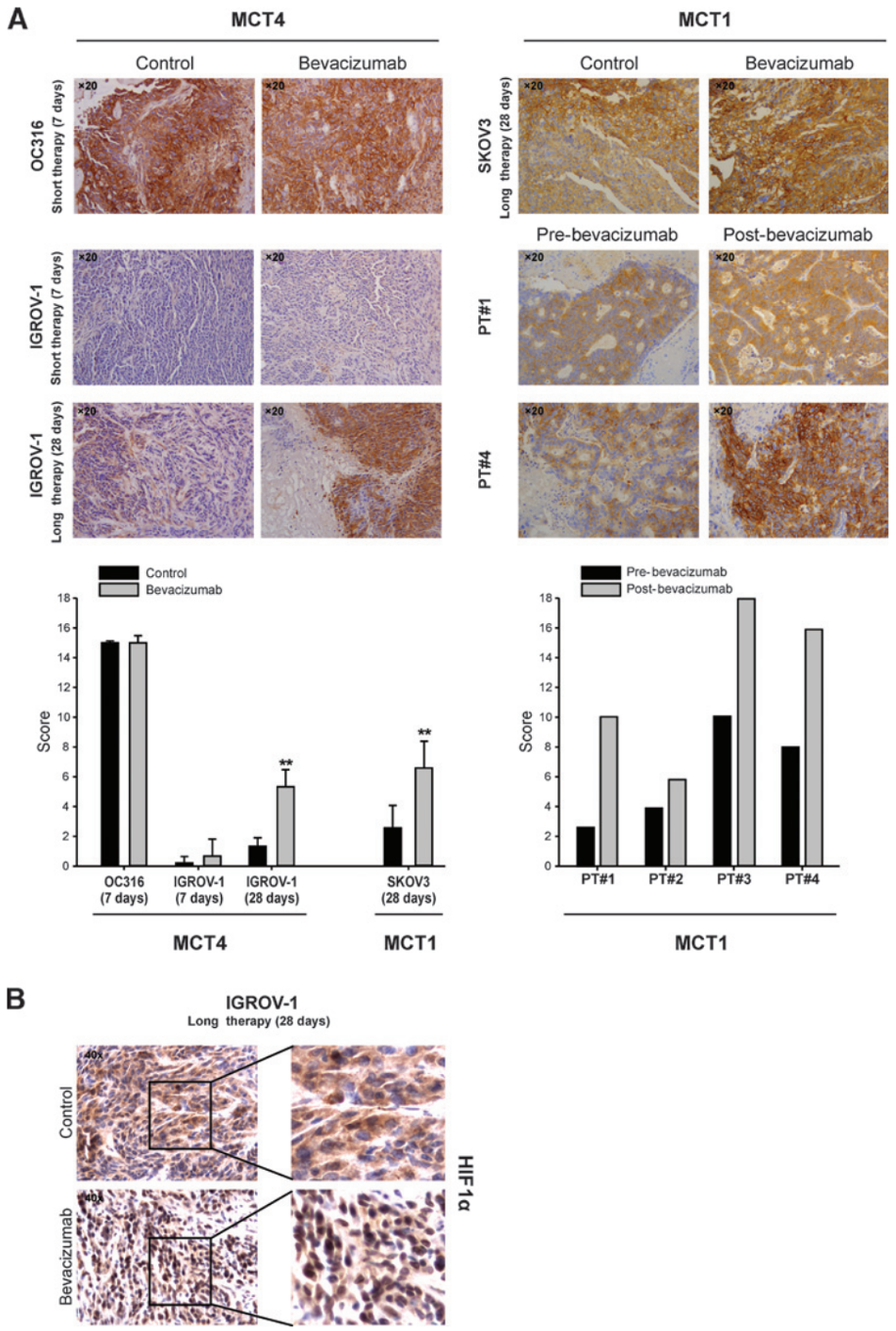

Figure 2.
Upregulation of *in situ* markers of the glycolytic phenotype as a consequence of sustained anti-VEGF therapy. A, expression of lactic acid transporters (MCT1 and MCT4) in tumor xenografts treated for 7 or 28 days with anti-VEGF mAb or liver metastatis of colorectal cancer patients treated with chemotherapy plus bevacizumab. Post-bevacizumab clinical samples were collected 7 to 12 months after administration of anti-VEGF therapy. Top, representative pictures; semiquantitative analysis of MCT1 and MCT4 expression is shown in the bottom (in the case of experimental tumors, 5 samples for group). Immunoreactivity was scored for both the intensity and the proportion of cells staining; intensity was given scores of 0 to 3 (0, no staining; 1, light staining; 2, moderate staining; 3, strong staining) and proportion was given scores of 1 to 6 (1, 0%–4%; 2, 5%–20%; 3, 21%–40%; 4, 41%–60%; 5, 61%–80%; 6, 81%–100%). The two scores were multiplied to obtain the final result of 0–18. Further details can be found in Supplementary Materials and Methods. **, $P < 0.01$, *t* test. B, representative pictures of HIF1α staining in control versus anti-VEGF-treated tumors showing increased nuclear expression of HIF1α in IGROV-1 tumors treated for 28 days with anti-VEGF mAb.

significantly higher glucose consumption and lactate production rates compared with *ex vivo* cultures from control tumors (Fig. 4A), along with increased cell death under glucose starvation, suggesting selection of glucose-addicted cells (Fig. 4B). We also found increased expression of several glycolysis-associated transcripts including *GLUT3*, *PFK*, *LDHA*, and *MCT4* transcript (Fig. 4C) and protein (Supplementary Fig. S5). Stimulated by these findings, we performed bioenergetic analysis of *ex vivo* cultures of IGROV-1 tumors. Parental IGROV-1 cells, which were previously characterized by the same technique (27), were used as controls. Notably, growth in mice as tumor xenografts did not change *per se* the bioenergetic features of IGROV-1 cells, whereas after anti-VEGF treatment, cells became much more glycolytic (Fig. 4D). In

Published OnlineFirst November 7, 2014; DOI: 10.1158/0008-5472.CAN-13-2037

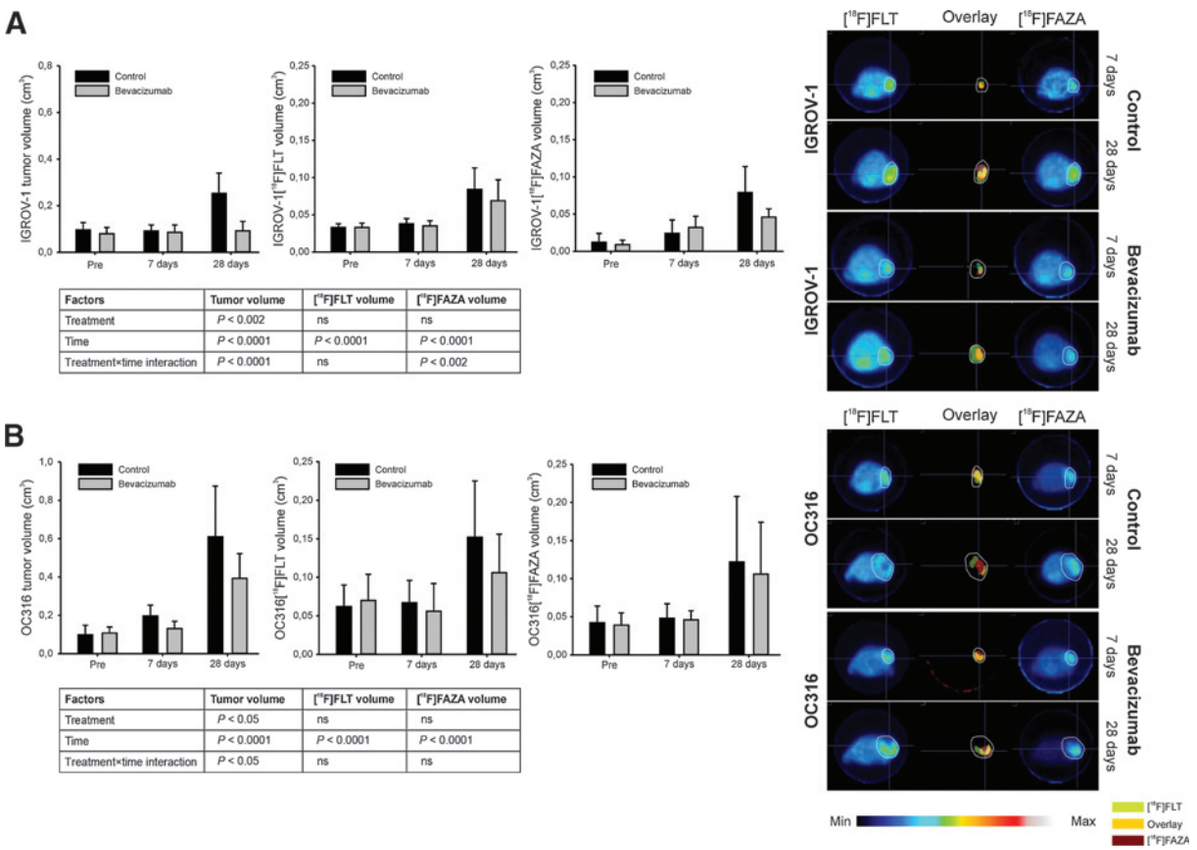

Figure 3.
Effect of anti-VEGF treatment on F[^{18}F]FLT and [^{18}F]FAZA uptake in tumors measured by PET. Measurement of tumor volume and PET images of IGROV-1 (A) and OC316 xenografts (B). Left, tumor volume obtained by measurement with caliper and the volume of [^{18}F]FLT and [^{18}F]FAZA distribution obtained by PET before and at 7 and 28 days after anti-VEGF treatment. Data are expressed as mean ± SD and were analyzed by two-way ANOVA followed by the Bonferroni *post hoc* test for multiple comparisons (tables). Right, representative transaxial PET images from [^{18}F]FLT and [^{18}F]FAZA and the overlay image of [^{18}F]FLT and [^{18}F]FAZA masks in the same mice (control and bevacizumab treated) at 7 and 28 days after therapy initiation. White lines, tumor volume. In overlay images, green color represents [^{18}F]FLT uptake, red color represents [^{18}F]FAZA uptake, and yellow color represents codistribution of both radiopharmaceuticals.

fact, OCR and ECAR did not substantially change in IGROV-1 cells after formation of tumor xenografts (compare wt and control IGROV-1 traces in the left and right panels of Fig. 4D), whereas treatment with bevacizumab (i) strongly inhibited OCR, and the effect of the ATP synthase inhibitor oligomycin indicated a specific downmodulation of coupled respiration, i.e., the fraction of oxygen consumption coupled to ATP synthesis; (ii) abolished any respiratory reserve, as the uncoupler FCCP, which at the reported concentration stimulates the maximal OCR, could not further increase oxygen consumption with respect to the basal value; this observation implies that cells acquire a Warburg phenotype, as they must utilize glycolytic ATP for any energy demand that exceeds their basal respiratory activity; (iii) increased ECAR, also after inhibition of respiratory complexes by rotenone/antimycin, which indicates that glycolysis is enhanced and scarcely funneled towards the Krebs cycle, leading to an enhancement of pyruvate conversion into lactate. This latter observation is in accordance with increased lactate production measured in supernatants of cultures obtained from anti–VEGF-treated mice (Fig. 4A) and with increased LDHA and *MCT4* expression levels (Fig. 4C). Overall, these results show that anti-VEGF therapy selected a highly glycolytic subpopulation of tumor cells, a conclusion further supported by bioenergetic analysis of *ex vivo* cultures of OC316 tumors, which became resistant to anti-VEGF therapy (Supplementary Fig. S7).

Mechanistically, we measured decreased expression of the mitochondrial complex NDUFS1 in cell cultures established from bevacizumab-treated tumors as well as reduced mitochondrial mass (Fig. 4E), which is consistent with decreased mitochondrial respiration. On the other hand, we did not detect increased HIF1α activity in normoxic cultures of IGROV-1 cells compared with the parental cell line (Supplementary Fig. S6A), indicating that these metabolic changes were not caused by persistent HIF1α signaling. Moreover, c-MYC, pAKT (Ser473 and Thr308) and pAMPK (Thr172) protein levels were comparable in *ex vivo* cultures from anti–VEGF-treated and control tumors (Supplementary Fig. S6B and S6C), suggesting that these well-established regulators of the Warburg effect (10) did not account for increased aerobic glycolysis.

Published OnlineFirst November 7, 2014; DOI: 10.1158/0008-5472.CAN-13-2037

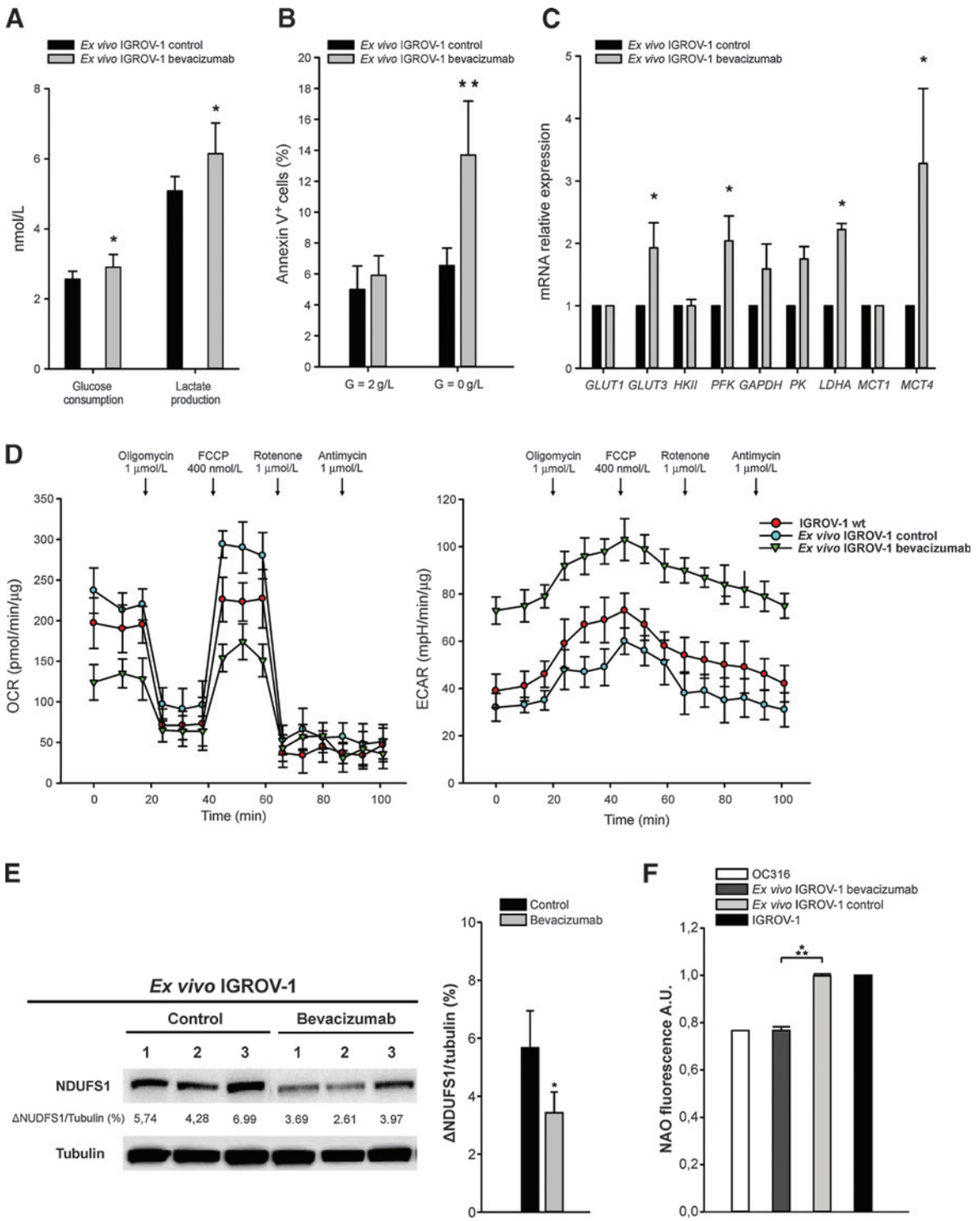

Figure 4.
Stable upmodulation of the glycolytic phenotype following anti-VEGF therapy. A, measurement of glucose consumption and lactic acid production by *ex vivo* cultures of IGROV-1 cells established from IGROV-1 tumors untreated (control) or treated for 28 days with anti-VEGF therapy (bevacizumab). Average volumes of control and bevacizumab tumors at sacrifice were 442.29 ± 197.19 mm^3 and 90.83 ± 80.00 mm^3, respectively. *Ex vivo* cultures were maintained in flasks at least 10 to 15 days before analysis. Cells were plated in P6 wells at 1.5 × 10^5 cells/well, incubated for 72 hours *in vitro* under normoxic conditions, and metabolic parameters were quantified by an automated analyzer. Mean ± SD values of five different samples for each group is shown. *, $P < 0.05$, *t* test. B, measurements of apoptosis by Annexin V staining of *ex vivo* cultures of IGROV-1 cells under glucose starvation. Columns report the mean values ± SD of five different samples for each group. **, $P < 0.01$, *t* test. (*Continued on the following page.*)

Published OnlineFirst November 7, 2014; DOI: 10.1158/0008-5472.CAN-13-2037

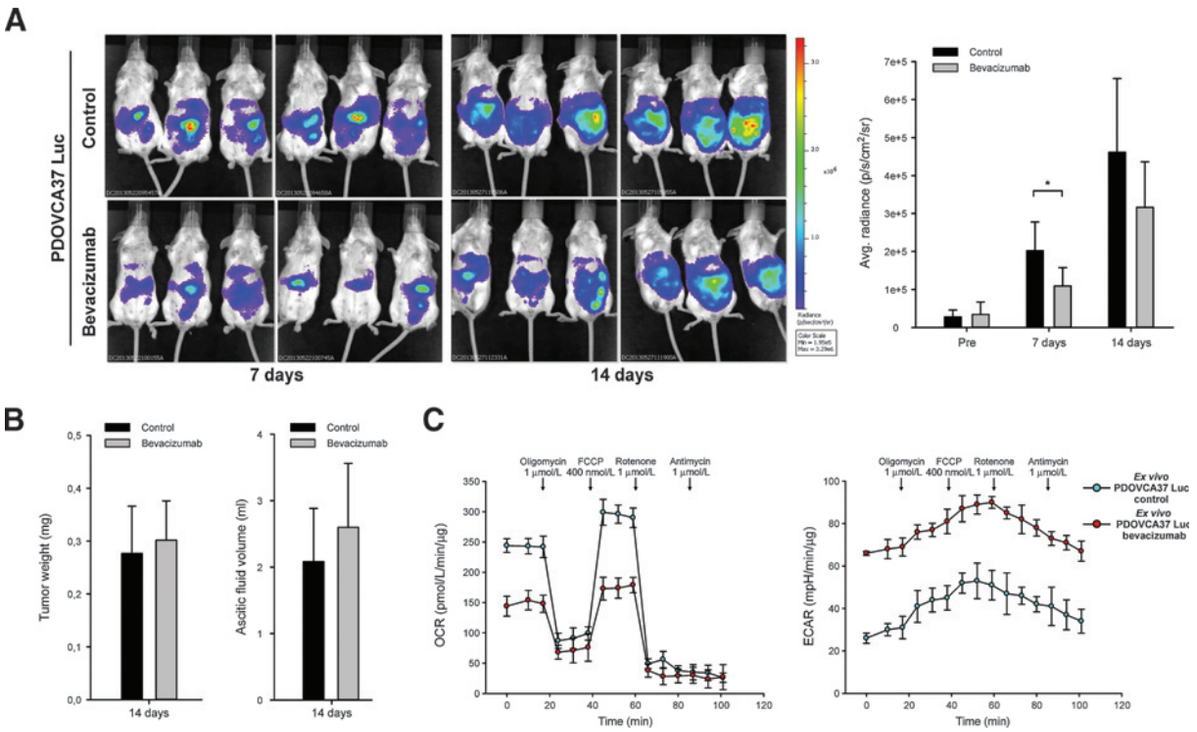

Figure 5.
Resistance to anti-VEGF therapy is associated with stable upmodulation of the glycolytic phenotype in patient-derived ovarian cancer xenografts. A, In order to track resistance to bevacizumab by optical imaging, PDOVCA37 cells were labeled with the luciferase gene and intraperitoneally injected into SCID mice (1×10^6 cells/mouse; $n = 6$ mice/group). When tumors became detectable by IVIS imaging (pre), mice were treated with bevacizumab (100 μg/dose administered every 2–3 days) for 2 weeks, until resistance appeared. Left, representative images acquired at 7 and 14 days after anti-VEGF treatment of six representative control and six bevacizumab-treated mice. Right, quantitative analysis of luciferase activity at various time points of measurement ($n = 6$ mice/group). Statistically significant differences in average radiance in the two groups of samples are indicated (*, $P < 0.05$, t test). B, columns indicate tumor weight and ascitic fluid volume of control and bevacizumab-treated tumors at sacrifice. C, bioenergetic analysis of *ex vivo* cultures of PDOVCA37 tumors. Representative OCR and ECAR traces obtained from monolayers of PDOVCA37 cells obtained from mouse xenografts untreated (control) or treated with anti-VEGF mAb (bevacizumab). Subsequent additions of the ATP synthase inhibitor oligomycin, of the uncoupler FCCP, of the ETC complex I inhibitor rotenone, and of the respiratory complex III inhibitor antimycin A were carried out. Data are mean ± SD values of ten replicates normalized to protein content. The experiment was repeated in five independent *ex vivo* cultures per group with similar results.

Anti-VEGF therapy causes a metabolic shift in clinically relevant tumor models

To strengthen these findings, we treated with bevacizumab a patient-derived ovarian cancer xenograft, which was tagged with the luciferase gene to enable noninvasive monitoring of tumor growth by optical imaging. Following an initial response, mainly consisting of reduced tumor burden, tumors became substantially resistant to VEGF blockade, as shown by optical imaging and measurements of tumor weight and volume of ascitic fluid at sacrifice (Fig. 5A and B). As found in the subcutaneous tumor models, metabolic flux analysis of *ex vivo* cultures established from these bevacizumab-treated tumors showed increased ECAR and reduced OCR compared with cultures from control tumors (Fig. 5C).

To rule out the possibility that these metabolic changes could only occur in the context of xenograft models, we validated our hypothesis in the BALB-neuT transgenic model of breast cancer (18). To this end, we treated 20-week-old BALB-neuT mice bearing measurable breast tumors (Supplementary Fig. S8A) with B20-4.1.1, an antibody neutralizing both human and mouse

(*Continued.*) C, quantitative RT-PCR analysis of glycolysis-associated transcripts in *ex vivo* cultures from IGROV-1 tumors. Columns show mean ± SD values of duplicate determinations of four samples for each group. *, $P < 0.05$, t test. Expression levels of the various transcripts in *ex vivo* IGROV-1 control samples were set at 1 to calculate relative variations. D, bioenergetic analysis of *ex vivo* cultures of IGROV-1 tumors. Representative OCR and ECAR traces obtained from monolayers of IGROV-1 cells either kept in culture, or obtained from mouse xenografts untreated (control) or treated with anti-VEGF mAb (bevacizumab). Subsequent additions of the ATP synthase inhibitor oligomycin, of the uncoupler FCCP, of the ETC complex I inhibitor rotenone, and of the respiratory complex III inhibitor antimycin A were carried out. Data are mean ± SD values of ten replicates normalized to protein content. The experiment was repeated in five independent *ex vivo* cultures per group with similar results. E, Western blot analysis of NDUFS1 levels in *ex vivo* cultures of IGROV-1 tumors. Tubulin was used as loading control. Left, three representative tumors per group are shown. Right, columns report the mean values ± SD of NDUFS1/Tubulin in all samples analyzed ($n = 5$ *ex vivo* IGROV-1 bevacizumab and $n = 4$ control samples). *, $P < 0.05$, t test. F, quantification of mitochondrial mass by staining with NAO in *ex vivo* bevacizumab or *ex vivo* control IGROV-1 cells. Parental IGROV-1 and OC316 cells were used as controls. Columns report the mean values ± SD of four different samples for each group. ***, $P < 0.001$, t test.

Published OnlineFirst November 7, 2014; DOI: 10.1158/0008-5472.CAN-13-2037

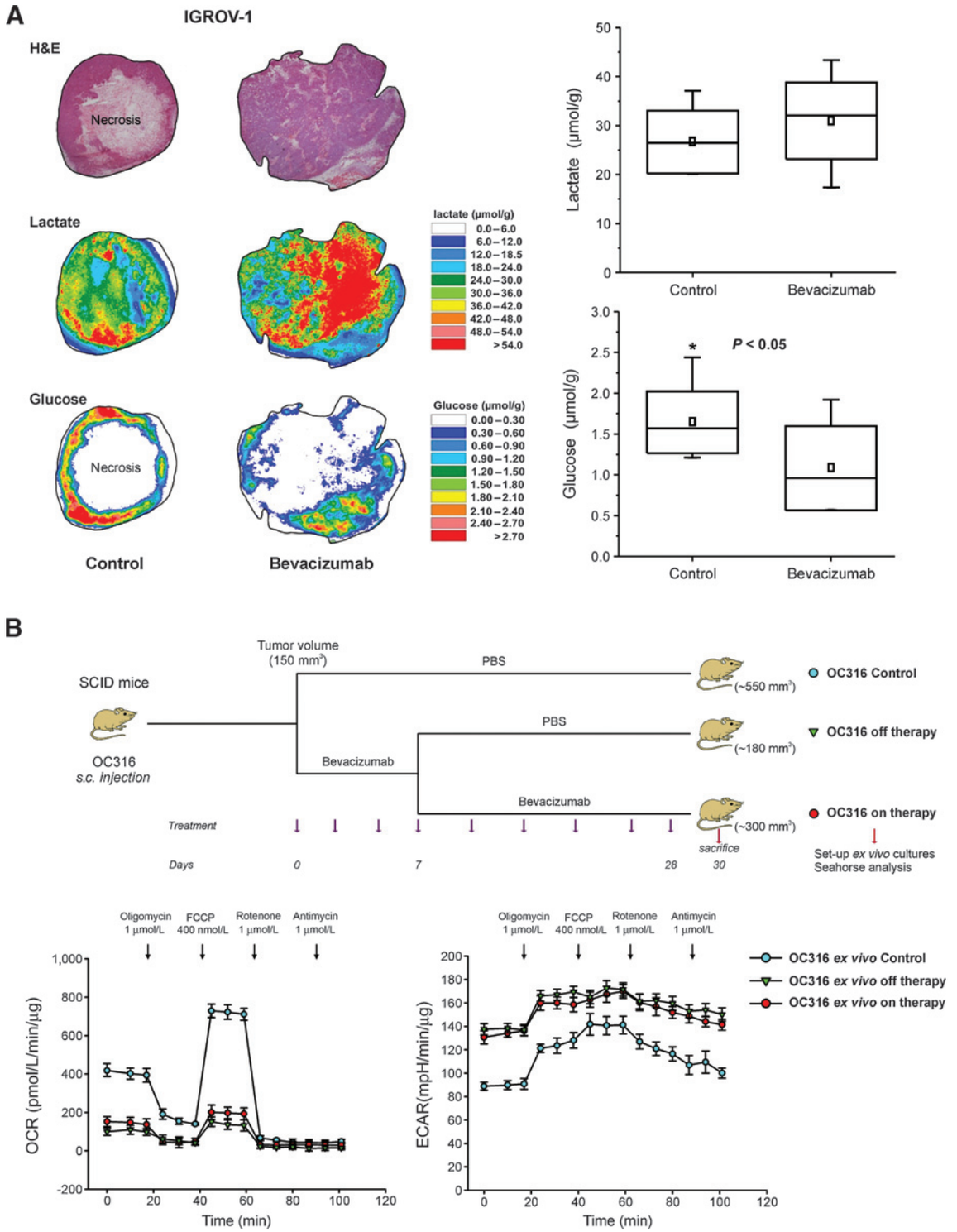

Figure 6.
The metabolic shift induced by anti-VEGF therapy is stable *in vivo*. A, quantification of lactate and glucose levels in IGROV-1 tumor xenografts by imBI. Left, hematoxylin and eosin (H&E) staining and color-coded distributions of lactate and glucose in sequential cryosections from representative tumors. As some tumors contain large central necrosis, glucose was at background levels within these large central areas. However, high glucose concentrations are clearly seen in the tumor periphery. This nicely illustrates the importance of structure-associated data acquisition with imBI. The concentration values were color-coded, with each color corresponding to a defined concentration range in μmol/g. (*Continued on the following page.*)

Published OnlineFirst November 7, 2014; DOI: 10.1158/0008-5472.CAN-13-2037

VEGF (20). Measurements of tumor volume and number of tumors per mouse showed that in this HER-2–driven spontaneous tumor model antiangiogenic therapy delayed tumor growth for about 24 days, followed by secondary resistance (Supplementary Fig. S8B). When *ex vivo* cultures of anti–VEGF-treated tumors were analyzed, increased ECAR, and reduced OCR were measured compared with *ex vivo* cultures from control tumors (Supplementary Fig. S8C).

Altogether, metabolic analysis in four different tumor models strongly support the conclusion that anti-VEGF therapy causes stable modulation of aerobic glycolysis in tumor cells.

Anti–VEGF-treated tumor cells maintain increased glycolysis *in vivo*, are highly tumorigenic, and show resistance to anti-VEGF therapy *in vivo*

To investigate whether upregulation of the glycolytic phenotype was stable and it was maintained *in vivo*, we subcutaneously injected tumor cells from *ex vivo* cultures of IGROV-1 tumors into naïve SCID mice. Measurement of glucose and lactate levels by imBI analysis disclosed significantly lower glucose levels and a trend towards higher lactate concentrations in tumors formed by IGROV-1 cells from anti–VEGF-treated mice compared with control tumors (Fig. 6A).

To strengthen these findings, we also investigated whether interruption of anti-VEGF therapy would affect the glycolytic phenotype of tumor cells. To this end, 7 days after anti-VEGF treatment mice bearing established OC316 xenografts were randomized to either continue for additional 21 days (on therapy group) or interrupt (off therapy group) anti-VEGF treatment (Fig. 6B). Seahorse analysis of *ex vivo* cultures from these tumors disclosed that even short-term anti-VEGF therapy is associated with increased glycolytic activity in the OC316 model. Moreover, similar metabolic profiles were found in "on therapy" versus "off therapy" samples, indicating that interruption of anti-VEGF therapy did not reverse the highly glycolytic phenotype associated with antiangiogenic therapy (Fig. 6B).

Finally, we investigated whether this metabolic switch was associated with distinctive patterns of tumor growth and response to anti-VEGF therapy. Accelerated kinetics of tumor growth was observed following injection of IGROV-1 cells from anti–VEGF-treated tumors (Fig. 7A), a finding that was confirmed also in the case of OC316 tumors (Fig. 7A). Notably, tumors formed by comparatively highly glycolytic IGROV-1 or OC316 cells from bevacizumab-treated mice were substantially less responsive to VEGF blockade compared with control tumors (Fig. 7B), thus indicating that these cell-autonomous metabolic traits confer resistance to VEGF blockade.

Cell tracing studies support *in vivo* selection of highly glycolytic tumor cells by anti-VEGF therapy

Finally, to determine whether tumor cells bearing highly glycolytic features are positively selected by anti-VEGF therapy, we performed cell tracing studies. In these experiments, we subcutaneously injected SCID mice with mixtures of tumor cells labeled by a fluorescent reporter (EGFP). MIX1 and MIX2 were obtained by *in vitro* mixing of unlabeled IGROV-1 cells in a 1:1 proportion with $EGFP^+$ bevacizumab-treated (highly glycolytic) or control (poorly glycolytic) IGROV-1 cells, respectively. Thirty-five to 43 days later, when average tumor volume was approximately 100 mm^3 (Fig. 7C), mice were either sacrificed or treated with bevacizumab according to the usual schedule for 28 days. The percentage of $EGFP^+$ cells in tumors was measured by flow cytometry either before or after anti-VEGF therapy. As shown in Fig. 7D, in the case of MIX2 we found 28.43% $\pm$ 8.36% $EGFP^+$ cells in pre-bevacizumab tumor samples and these numbers changed minimally after anti-VEGF therapy (29.13% $\pm$ 5.22%). The percentage of $EGFP^+$ cells was reduced compared with the preinjection value (50%), probably due to partial downregulation of transgene expression. In contrast, in the case of MIX1, the percentage of $EGFP^+$ cells in tumors significantly increased after anti-VEGF therapy (37.85% $\pm$10.33%) with respect to pretreatment values (18.95% $\pm$ 3.22%; Fig. 7D). This result supports the hypothesis that anti-VEGF therapy fosters selection of tumor cells endowed with certain metabolic features.

Discussion

Several hypotheses have been proposed to explain resistance to antiangiogenic therapies (3, 4). As these drugs generally lack direct cytotoxic effects, their therapeutic activity is assumed to be due to their indirect effects, such as depletion of oxygen and key substrates needed to sustain tumor cell proliferation and growth (29). As tumors exhibit heterogeneous metabolic profiles (30), we sought to investigate whether the metabolic phenotype of tumor cells might influence therapeutic responses to antiangiogenic drugs.

On the basis of our previous finding that glucose levels are dramatically impaired in experimental tumors treated with anti-VEGF therapy (14), we initially hypothesized that glucose-addicted tumors could better respond to antiangiogenic drugs. However, we observed that while various glucose-dependent tumor xenografts are initially starved due to induction of large necrotic areas, they subsequently become rapidly resistant to VEGF blockade. This finding was confirmed by analysis of response to anti-VEGF therapy of xenografts formed by variants of IGROV-1 cells, which selectively differ in the levels of expression of *AMPK*, a serine-threonine kinase implicated in the regulation of the Warburg effect (26), although it should be considered that AMPK has pleiotropic effects on cell metabolism (31), in particular regulation of mTOR activity, which could also contribute to the results obtained.

Resistance to VEGF blockade was associated with selection of tumor cells with increased proliferation, as shown by [^{18}F]FLT PET analysis (Fig. 3) and also by measurement of cell proliferation in *ex vivo* cultures from bevacizumab-treated versus control tumors (Supplementary Fig. S4). In this respect, highly proliferative

(*Continued.*) Right, metabolite concentrations of lactate and glucose in tumors. Lactate and glucose values were calculated from nine and seven sections from anti–VEGF-treated or control tumors, respectively. B, interruption of anti-VEGF therapy does not reverse the highly glycolytic phenotype. Top, layout of the experiment: SCID mice bearing established subcutaneously OC316 xenografts (mean volume 150 mm^3) were treated for 7 days with bevacizumab (arrows) and then randomized to either stop (off therapy group) or continue (on therapy group) anti-VEGF therapy for additional 3 weeks. Control mice received PBS. At sacrifice, *ex vivo* cultures were established from tumors and analyzed by Seahorse. Bottom, metabolic flux analysis. Representative OCR and ECAR traces of *ex vivo* cultures of OC316 cells established from control, off therapy, and on therapy tumors. The experiment was repeated in five independent *ex vivo* cultures per group with similar results.

Published OnlineFirst November 7, 2014; DOI: 10.1158/0008-5472.CAN-13-2037

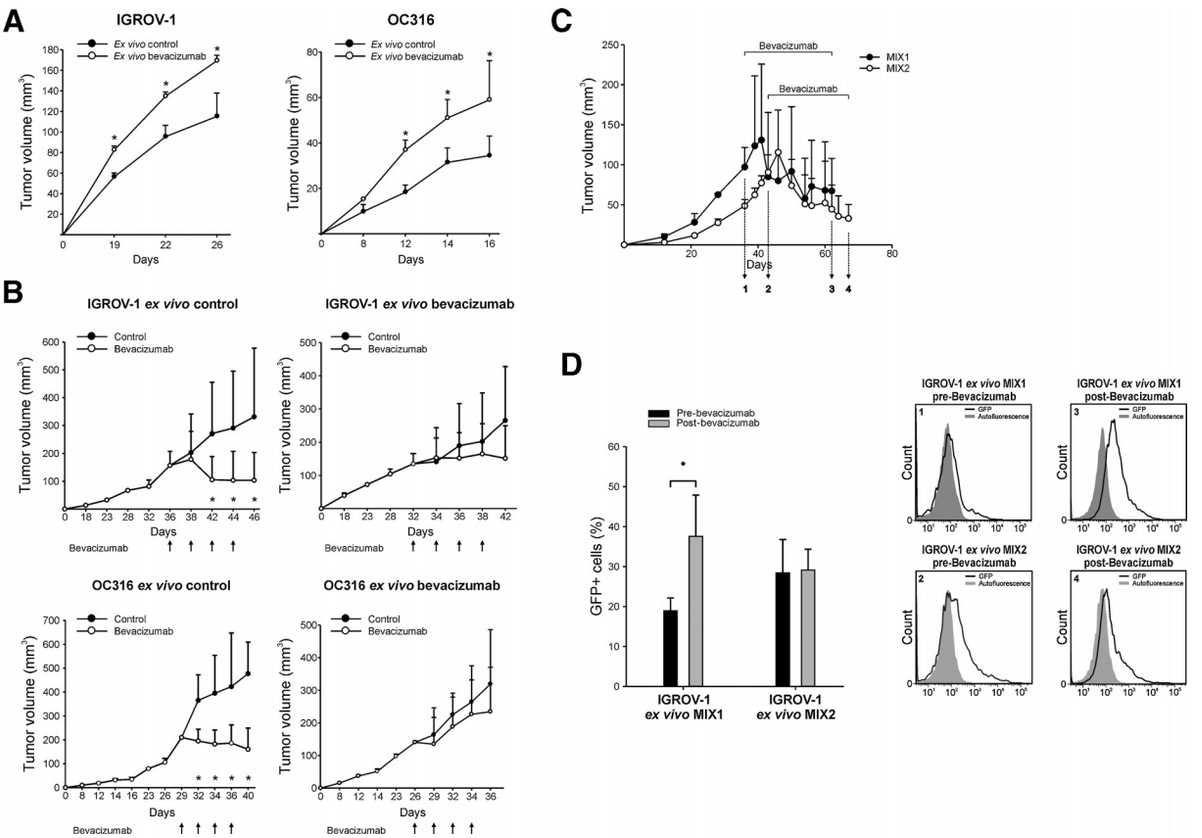

Figure 7.
Tumor cells from anti–VEGF-treated mice have increased tumorigenic capacity, are resistant to bevacizumab, and are positively selected by anti-VEGF therapy. A, kinetics of tumor development following subcutaneous injection of IGROV-1 (left) or OC316 (right) tumor cells (4×10^5 cells/flank) derived from bevacizumab-treated tumors compared with control tumors ($n = 5$ mice/group). *, $P < 0.05$, *t* test. B, effects of multiple injections of the anti-VEGF mAb bevacizumab (arrows, 100 μg/dose administered every 2–3 days) on tumor size. Tumor xenografts derived from *ex vivo* cultures of anti–VEGF-treated IGROV-1 or OC316 tumors are resistant to anti-VEGF therapy (right) compared with xenografts derived from control cells (left; $n = 5$ mice for group). *, $P < 0.05$, *t* test. C, kinetics of tumor development following subcutaneous injection of a 1:1 mix of EGFP-tagged IGROV-1 cells derived from bevacizumab-treated tumors and unlabeled control tumor cells (MIX1) or a 1:1 mix of EGFP-tagged IGROV-1 cells from control tumors and unlabeled control tumor cells (MIX2) and effects of the anti-VEGF mAb bevacizumab (100 μg/dose administered every 2–3 days) on tumor size. MIX1 and MIX2 tumors ($n = 4$ samples/group) were collected either before (time points 1 and 2 for MIX1 and MIX2, respectively) or after (time points 3 and 4 for MIX1 and MIX2, respectively) bevacizumab administration and the percentage of $EGFP^+$ cells in tumors was quantified by flow cytometry. D, tumor cells with peculiar metabolic features are positively selected by anti-VEGF therapy. Left, quantification of $EGFP^+$ IGROV-1 cells in MIX1 and MIX2 tumors before or after bevacizumab administration. Columns report the mean values ± SD of four different samples for each group. *, $P < 0.05$, *t* test. Right, representative histogram plots of $EGFP^+$ cells for each of the experimental groups (1, 2, 3, and 4) described in C.

tumor rims were previously reported following treatment of experimental tumors with vascular damaging drugs (32). Altogether, these results suggest that necrosis induced by anti-VEGF therapy triggers proliferation in the surviving tumor cells. Metabolic features of tumors, and in particular their glycolytic phenotype, have a substantial impact on the development of tumor necrosis following antiangiogenic treatment. This increased cellular turnover could accelerate Darwinian selection of a population of cells resistant to hypoxia and acidosis (33), thereby influencing the kinetics of secondary resistance.

On the other hand, other factors could also contribute to relapse, including recruitment by the necrotic tissue of circulating endothelial progenitor cells (34), macrophages, and other specialized myeloid cells releasing proangiogenic factors that could bypass VEGF neutralization (35). Indeed, some variations in tumor-associated myeloid cells, mainly reflecting increased levels of $CD11b^+/Gr1^+$ cells, were measured in tumors treated with anti-VEGF therapy (data not shown). Moreover, lactate, which accumulates in highly glycolytic tumors, is a pleomorphic tumor-promoting factor that stimulates angiogenesis by NFκB activation in endothelial cells (36). However, it should be noted that in our models microvessel density of anti–VEGF-resistant tumors was significantly reduced compared with controls, indicating that the tumor vasculature was still dependent on VEGF. Therefore, therapeutic resistance did not appear to be primarily related to renewed vascularization due to recruited myeloid cells or a switch to alternative angiogenic factors, as reported in other models of resistance to VEGF blockade (37–39).

Published OnlineFirst November 7, 2014; DOI: 10.1158/0008-5472.CAN-13-2037

We concede that the clinical relevance of these observations remains to be established. First of all, treatment-induced necrosis may eventually trigger an immune-mediated response in patients, which cannot be seen in immunodeficient mice, and this could restrain tumor growth. Moreover, bevacizumab is invariably given to patients in combination with chemotherapy and cytotoxic drugs that could potentially kill highly proliferating tumor cells resistant to anti-VEGF therapy, thus preventing tumor relapse (31).

The most important conclusion of this study, grounded on experimental work in both tumor xenografts and a spontaneous tumor model, is that antiangiogenic therapy favors emergence of a glucose-dependent metabolic phenotype. This is likely promoted by chronic hypoxia and induction of the HIF1α-driven transcriptional program, which involves activation of glycolysis (28). Indeed, we observed a dramatic increment in tumor hypoxic regions with [^{18}F]FAZA PET and also nuclear accumulation of HIF1α, which could drive the metabolic switch in the tumor microenvironment and favor evasive mechanisms (40). However, the stable metabolic changes measured *in vitro* were not due to stabilization of HIF1α levels in tumor cells, increased c-MYC and pAKT levels, or loss of AMPK activity (Supplementary Fig. S6). The discrepancy between HIF1α expression levels *in vivo* versus *in vitro* conditions indicates that accumulation of this transcription factor in tumor cells remains hypoxia-dependent.

Although increased expression of glycolysis-associated markers following bevacizumab has been observed in other studies (41), here we show for the first time that anti-VEGF therapy caused a stable modification of the metabolic phenotype of the tumor. This was supported by (i) the finding that *ex vivo* cultures from anti–VEGF-treated tumors had different metabolic features with respect to those established from control tumors (Fig. 4), (ii) results of imBI analysis, which showed that xenografts formed by tumor cells from anti–VEGF-treated mice maintained a highly glycolytic phenotype (Fig. 6A), and (iii) results of on/off therapy experiments (Fig. 6B).

These stable metabolic modifications could be due to either selection of a pre-existing subpopulation of highly glycolytic tumor cells or, alternatively, be accounted for by epigenetic reprogramming of cell metabolism, as shown in the model presented in Supplementary Fig. S9. With regard to the first possibility, angiogenesis inhibitors alter the environment through increased hypoxia, glucose deprivation, and acidosis, which produce strong Darwinian forces that rapidly promote adaptive phenotypes (33). In this respect, it has been reported that glucose deprivation provides a strong selection for activated oncogenes, such as *KRAS* (42). Moreover, Xu and colleagues recently described mitochondrial defects in *ex vivo* cultures of LoVo cells from bevacizumab-treated tumors (43), and we also found reduced mitochondrial mass and decreased expression of NDUFS1, a component of respiratory complex I, in *ex vivo* cultures of bevacizumab-treated IGROV-1 cells (Supplementary Fig. S5). In support of this possibility, cell tracing experiments demonstrated that EGFP-labeled highly glycolytic tumor cells are positively selected by anti-VEGF therapy (Fig. 7).

Alternatively, new findings have uncovered regulation of glucose metabolism by sirtuins 1, 3, 4, and 6 (44), and epigenetic variations in sirtuins levels could possibly contribute to the phenomenon observed. In preliminary experiments, however, we found that SIRT3, SIRT4, and SIRT6 were barely expressed in IGROV-1 and OC316 cells, whereas SIRT1 was expressed at comparable levels in IGROV-1 and OC316 cells from bevacizumab-treated tumors compared with control cultures (not shown). Therefore, although other epigenetic mechanisms could be involved, dysregulated expression of sirtuins is not likely to account for the metabolic shift observed in these tumor models.

Metabolic evolution of tumors following antiangiogenic therapy is a novel concept that could have relevant translational implications. A metabolic shift involving downregulation of genes involved in the tricarboxylic acid cycle, decreased AMPK and PTEN protein levels, upregulation of the pentose phosphate pathway was recently described in aggressive renal cell carcinoma (45) and fits with increased kinetics of tumor growth by anti–VEGF-treated tumor cells observed in this study. Moreover, as glucose-addicted tumors have dismal prognosis (25, 46) and could be relatively resistant to cytotoxic therapies (47, 48), this phenomenon might contribute to explain the relatively short-term benefits of antiangiogenic therapy.

Disclosure of Potential Conflicts of Interest

No potential conflicts of interest were disclosed.

Authors' Contributions

Conception and design: M. Curtarello, M. Plebani, W. Mueller-Klieser, R.M. Moresco, S. Indraccolo

Development of methodology: M. Curtarello, S. Todde, W. Mueller-Klieser

Acquisition of data (provided animals, acquired and managed patients, provided facilities, etc.): M. Curtarello, E. Zulato, G. Nardo, S. Valtorta, A. Msaki, A. Pasto, A. Rasola, L. Persano, F. Ciccarese, H. Schroer, S. Walenta, W. Mueller-Klieser

Analysis and interpretation of data (e.g., statistical analysis, biostatistics, computational analysis): M. Curtarello, E. Zulato, G. Nardo, S. Valtorta, G. Guzzo, E. Rossi, G. Esposito, A. Pasto, A. Rasola, F. Ciccarese, R. Bertorelle, M. Plebani, S. Walenta

Writing, review, and/or revision of the manuscript: M. Curtarello, E. Zulato, G. Nardo, S. Valtorta, A. Msaki, M. Plebani, S. Walenta, W. Mueller-Klieser, R.M. Moresco, S. Indraccolo

Administrative, technical, or material support (i.e., reporting or organizing data, constructing databases): E. Rossi

Study supervision: A. Amadori, R.M. Moresco, S. Indraccolo

Acknowledgments

The authors thank Prof. Guido Forni for providing the BALB-neuT mice, Dr. Isabella Raccagni for PET studies and image analysis, Dr. Valeria Masiello and Cristina Monterisi for radiochemical production and quality control, Dr. Paola Fogar for help in measurements of glucose and lactate in supernatants, and Dr. Valentina Serafin for assistance in preparation of tumor samples for immunohistochemical analysis. The authors also thank Genentech for kindly providing the anti-VEGF mAb B20-4.1.1.

Grant Support

This work was supported by grants from AIRC (IG grants 14295 and 14032), Progetto d'Ateneo 2010 (S. Indraccolo), Progetto d'Ateneo 2012 (A. Rasola), PRIN (grant 2009P5JPT4_003 and 2010MCLPLB_003) and from the Deutsche Forschungsgemeinschaft DFG (Mu 576/15-1 and SA 1749/3-1) and from the Mainzer Forschungsfoerderungsprogramm MAIFOR (#8277000; W. Mueller-Klieser). This project was also partially supported by grants of

the Italian Minister of University: Progetto Premiale Medicina Personalizzata and Sysbionet, (Italian Research Infrastructures of the Italian *ESFRI* roadmap; R.M. Moresco).

The costs of publication of this article were defrayed in part by the payment of page charges. This article must therefore be hereby marked *advertisement* in accordance with 18 U.S.C. Section 1734 solely to indicate this fact.

Received July 18, 2013; revised September 8, 2014; accepted October 13, 2014; published OnlineFirst November 7, 2014.

References

1. Heath VL, Bicknell R. Anticancer strategies involving the vasculature. Nat Rev Clin Oncol 2009;6:395–404.
2. Ellis LM, Hicklin DJ. VEGF-targeted therapy: mechanisms of anti-tumour activity. Nat Rev Cancer 2008;8:579–91.
3. Bergers G, Hanahan D. Modes of resistance to antiangiogenic therapy. Nat Rev Cancer 2008;8:592–603.
4. Ellis LM, Hicklin DJ. Pathways mediating resistance to vascular endothelial growth factor-targeted therapy. Clin Cancer Res 2008;14:6371–5.
5. Bottsford-Miller JN, Coleman RL, Sood AK. Resistance and escape from antiangiogenesis therapy: clinical implications and future strategies. J Clin Oncol 2012;30:4026–34.
6. Jahangiri A, De Lay M, Miller LM, Carbonell WS, Hu YL, Lu K, et al. Gene expression profile identifies tyrosine kinase c-met as a targetable mediator of antiangiogenic therapy resistance. Clin Cancer Res 2013;19:1773–83.
7. Tennant DA, Duran RV, Gottlieb E. Targeting metabolic transformation for cancer therapy. Nat Rev Cancer 2010;10:267–77.
8. Iorio E, Ricci A, Bagnoli M, Pisanu ME, Castellano G, Di Vito M, et al. Activation of phosphatidylcholine cycle enzymes in human epithelial ovarian cancer cells. Cancer Res 2010;70:2126–35.
9. DeBerardinis RJ, Lum JJ, Hatzivassiliou G, Thompson CB. The biology of cancer: metabolic reprogramming fuels cell growth and proliferation. Cell Metab 2008;7:11–20.
10. Dang CV. Links between metabolism and cancer. Genes Dev 2012;26:877–90.
11. Sciacovelli M, Guzzo G, Morello V, Frezza C, Zheng L, Nannini N, et al. The mitochondrial chaperone TRAP1 promotes neoplastic growth by inhibiting succinate dehydrogenase. Cell Metab 2013;17:988–99.
12. Bohndiek SE, Kettunen MI, Hu DE, Brindle KM. Hyperpolarized (13)C spectroscopy detects early changes in tumor vasculature and metabolism after VEGF neutralization. Cancer Res 2012;72:854–64.
13. Keunen O, Johansson M, Oudin A, Sanzey M, Rahim SA, Fack F, et al. Anti-VEGF treatment reduces blood supply and increases tumor cell invasion in glioblastoma. Proc Natl Acad Sci USA 2011;108:3749–54.
14. Nardo G, Favaro E, Curtarello M, Moserle L, Zulato E, Persano L, et al. Glycolytic phenotype and AMP kinase modify the pathologic response of tumor xenografts to VEGF neutralization. Cancer Res 2011;71:4214–25.
15. Favaro E, Nardo G, Persano L, Masiero M, Moserle L, Zamarchi R, et al. Hypoxia inducible factor-1alpha inactivation unveils a link between tumor cell metabolism and hypoxia-induced cell death. Am J Pathol 2008;173:1186–201.
16. Indraccolo S, Tisato V, Agata S, Moserle L, Ferrari S, Callegaro M, et al. Establishment and characterization of xenografts and cancer cell cultures derived from BRCA1$^{-/-}$ epithelial ovarian cancers. Eur J Cancer 2006;42:1475–83.
17. Agnusdei V, Minuzzo S, Frasson C, Grassi A, Axelrod F, Satyal S, et al. Therapeutic antibody targeting of Notch1 in T-acute lymphoblastic leukemia xenografts. Leukemia 2014;28:278–88.
18. Cavallo F, Offringa R, van der Burg SH, Forni G, Melief CJ. Vaccination for treatment and prevention of cancer in animal models. Adv Immunol 2006;90:175–213.
19. Boggio K, Nicoletti G, Di Carlo E, Cavallo F, Landuzzi L, Melani C, et al. Interleukin 12-mediated prevention of spontaneous mammary adenocarcinomas in two lines of Her-2/neu transgenic mice. J Exp Med 1998;188:589–96.
20. Bagri A, Berry L, Gunter B, Singh M, Kasman I, Damico LA, et al. Effects of anti-VEGF treatment duration on tumor growth, tumor regrowth, and treatment efficacy. Clin Cancer Res 2010;16:3887–900.
21. Tehrani OS, Shields AF. PET imaging of proliferation with pyrimidines. J Nucl Med 2013;54:903–12.
22. Valtorta S, Belloli S, Sanvito F, Masiello V, Di Grigoli G, Monterisi C, et al. Comparison of 18F-Fluoroazomycin-Arabinofuranoside and 64Cu-Diacetyl-Bis(N4-Methylthiosemicarbazone) in preclinical models of cancer. J Nucl Med 2013;54:1106–12.
23. Mueller-Klieser W, Walenta S. Geographical mapping of metabolites in biological tissue with quantitative bioluminescence and single photon imaging. Histochem J 1993;25:407–20.
24. Sattler UG, Walenta S, Mueller-Klieser W. A bioluminescence technique for quantitative and structure-associated imaging of pyruvate. Lab Invest 2007;87:84–92.
25. Walenta S, Wetterling M, Lehrke M, Schwickert G, Sundfor K, Rofstad EK, et al. High lactate levels predict likelihood of metastases, tumor recurrence, and restricted patient survival in human cervical cancers. Cancer Res 2000;60:916–21.
26. Faubert B, Boily G, Izreig S, Griss T, Samborska B, Dong Z, et al. AMPK is a negative regulator of the Warburg effect and suppresses tumor growth *in vivo*. Cell Metab 2013;17:113–24.
27. Fabian C, Koetz L, Favaro E, Indraccolo S, Mueller-Klieser W, Sattler UG. Protein profiles in human ovarian cancer cell lines correspond to their metabolic activity and to metabolic profiles of respective tumor xenografts. FEBS J 2012;279:882–91.
28. Harris AL. Hypoxia–a key regulatory factor in tumour growth. Nat Rev Cancer 2002;2:38–47.
29. Kieran MW, Folkman J, Heymach J. Angiogenesis inhibitors and hypoxia. Nat Med 2003;9:1104
30. Vander Heiden MG. Targeting cancer metabolism: a therapeutic window opens. Nat Rev Drug Discov 2011;10:671–84.
31. Mihaylova MM, Shaw RJ. The AMPK signalling pathway coordinates cell growth, autophagy and metabolism. Nat Cell Biol 2011;13:1016–23.
32. Tozer GM, Kanthou C, Baguley BC. Disrupting tumour blood vessels. Nat Rev Cancer 2005;5:423–35.
33. Gillies RJ, Verduzco D, Gatenby RA. Evolutionary dynamics of carcinogenesis and why targeted therapy does not work. Nat Rev Cancer 2012;12:487–93.
34. Shaked Y, Ciarrocchi A, Franco M, Lee CR, Man S, Cheung AM, et al. Therapy-induced acute recruitment of circulating endothelial progenitor cells to tumors. Science 2006;313:1785–7.
35. Murdoch C, Muthana M, Coffelt SB, Lewis CE. The role of myeloid cells in the promotion of tumour angiogenesis. Nat Rev Cancer 2008;8:618–31.
36. Vegran F, Boidot R, Michiels C, Sonveaux P, Feron O. Lactate influx through the endothelial cell monocarboxylate transporter MCT1 supports an NF-kappaB/IL-8 pathway that drives tumor angiogenesis. Cancer Res 2011;71:2550–60.
37. Casanovas O, Hicklin DJ, Bergers G, Hanahan D. Drug resistance by evasion of antiangiogenic targeting of VEGF signaling in late-stage pancreatic islet tumors. Cancer Cell 2005;8:299–309.
38. Ebos JM, Lee CR, Christensen JG, Mutsaers AJ, Kerbel RS. Multiple circulating proangiogenic factors induced by sunitinib malate are tumor-independent and correlate with antitumor efficacy. Proc Natl Acad Sci USA 2007;104:17069–74.
39. Fernando NT, Koch M, Rothrock C, Gollogly LK, D'Amore PA, Ryeom S, et al. Tumor escape from endogenous, extracellular matrix-associated angiogenesis inhibitors by up-regulation of multiple proangiogenic factors. Clin Cancer Res 2008;14:1529–39.
40. Rapisarda A, Melillo G. Overcoming disappointing results with antiangiogenic therapy by targeting hypoxia. Nat Rev Clin Oncol 2012;9:378–90.
41. Kumar K, Wigfield S, Gee HE, Devlin CM, Singleton D, Li JL, et al. Dichloroacetate reverses the hypoxic adaptation to bevacizumab and enhances its antitumor effects in mouse xenografts. J Mol Med 2013;91:749–58.
42. Yun J, Rago C, Cheong I, Pagliarini R, Angenendt P, Rajagopalan H, et al. Glucose deprivation contributes to the development of KRAS pathway mutations in tumor cells. Science 2009;325:1555–9.

43. Xu J, Wang J, Xu B, Ge H, Zhou X, Fang JY. Colorectal cancer cells refractory to anti-VEGF treatment are vulnerable to glycolytic blockade due to persistent impairment of mitochondria. Mol Cancer Ther 2013;12:717–24.
44. Guarente L. The many faces of sirtuins: sirtuins and the Warburg effect. Nat Med 2014;20:24–5.
45. Creighton CJ, Morgan M, Gunaratne PH, Wheeler DA, Gibbs RA. Comprehensive molecular characterization of clear cell renal cell carcinoma. Nature 2013;499:43–9.
46. Walenta S, Schroeder T, Mueller-Klieser W. Lactate in solid malignant tumors: potential basis of a metabolic classification in clinical oncology. Curr Med Chem 2004;11:2195–204.
47. Zhao Y, Liu H, Liu Z, Ding Y, Ledoux SP, Wilson GL, et al. Overcoming trastuzumab resistance in breast cancer by targeting dysregulated glucose metabolism. Cancer Res 2011;71:4585–97.
48. Zhou M, Zhao Y, Ding Y, Liu H, Liu Z, Fodstad O, et al. Warburg effect in chemosensitivity: targeting lactate dehydrogenase-A re-sensitizes taxol-resistant cancer cells to taxol. Mol Cancer 2010;9:33.

Published OnlineFirst November 7, 2014; DOI: 10.1158/0008-5472.CAN-13-2037

Cancer Research

VEGF-Targeted Therapy Stably Modulates the Glycolytic Phenotype of Tumor Cells

Matteo Curtarello, Elisabetta Zulato, Giorgia Nardo, et al.

Cancer Res 2015;75:120-133. Published OnlineFirst November 7, 2014.

Suppl. Fig. 1

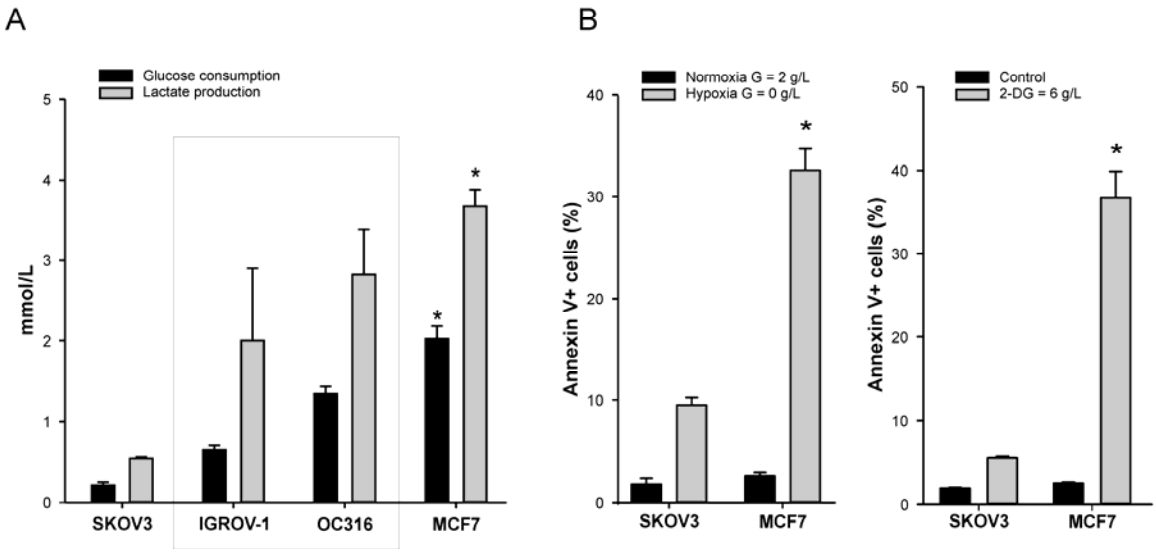
A
Glucose consumption
Lactate production
mmol/L
0
1
2
3
4
5
SKOV3
IGROV-1
OC316
MCF7
*
*
B
Normoxia G = 2 g/L
Hypoxia G = 0 g/L
Annexin V+ cells (%)
0
10
20
30
40
SKOV3
MCF7
*
Control
2-DG = 6 g/L
Annexin V+ cells (%)
0
10
20
30
40
50
SKOV3
MCF7
*

Suppl. Fig. 2

A

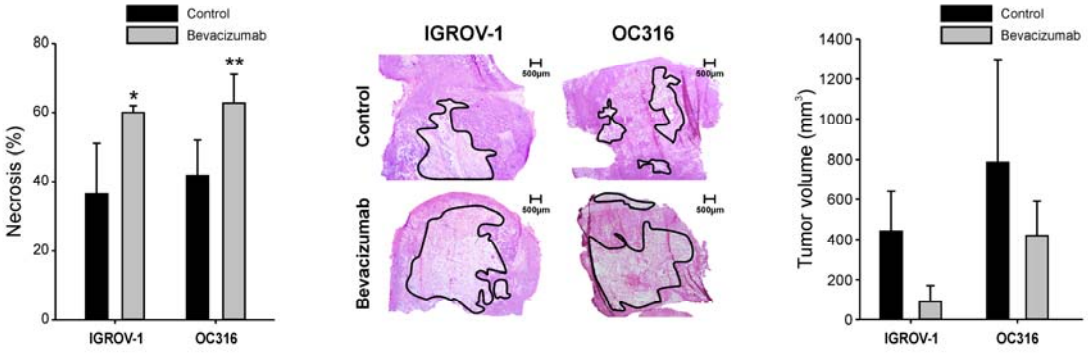

B

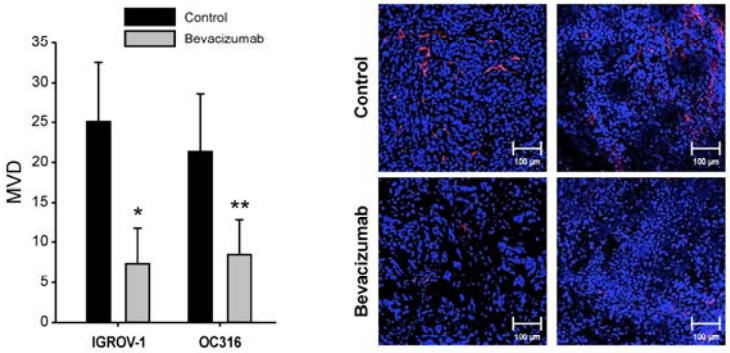

Suppl. Fig. 3

A

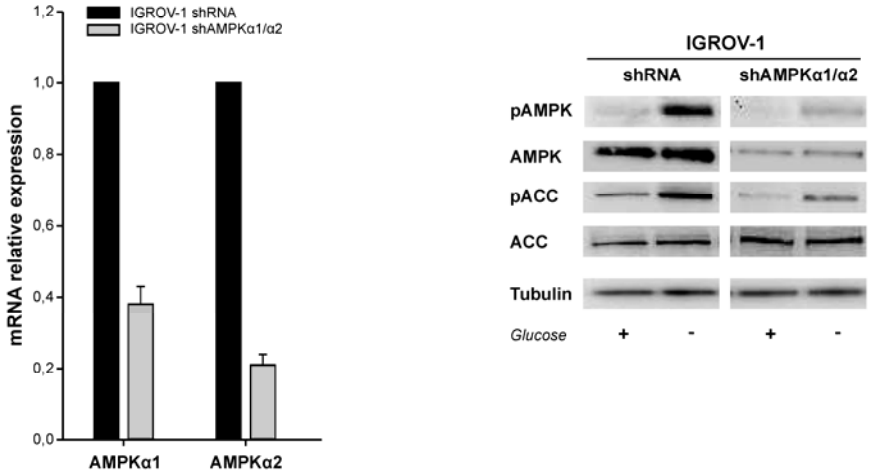

B

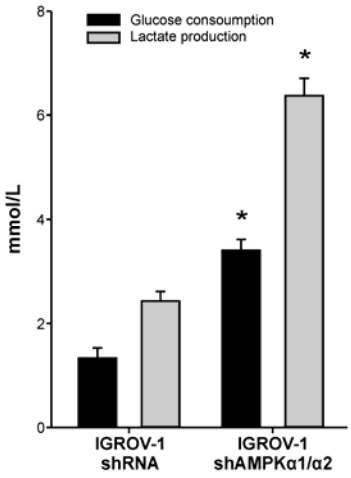

C

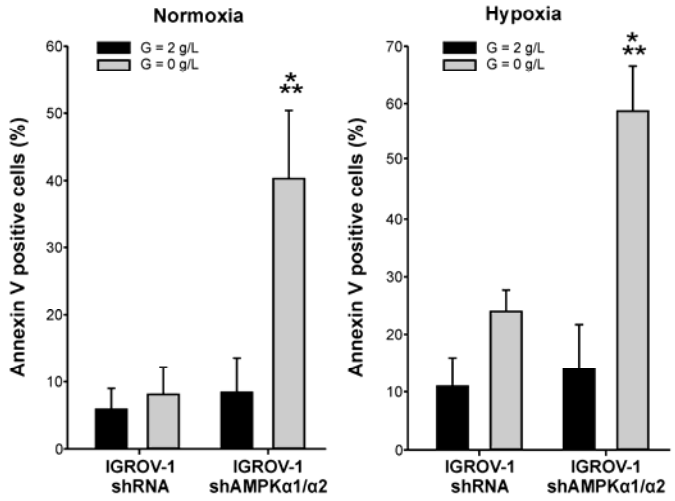

D

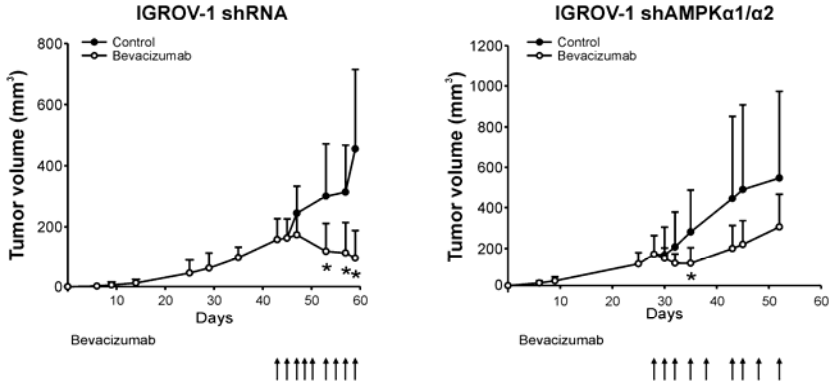

Suppl. Fig. 4

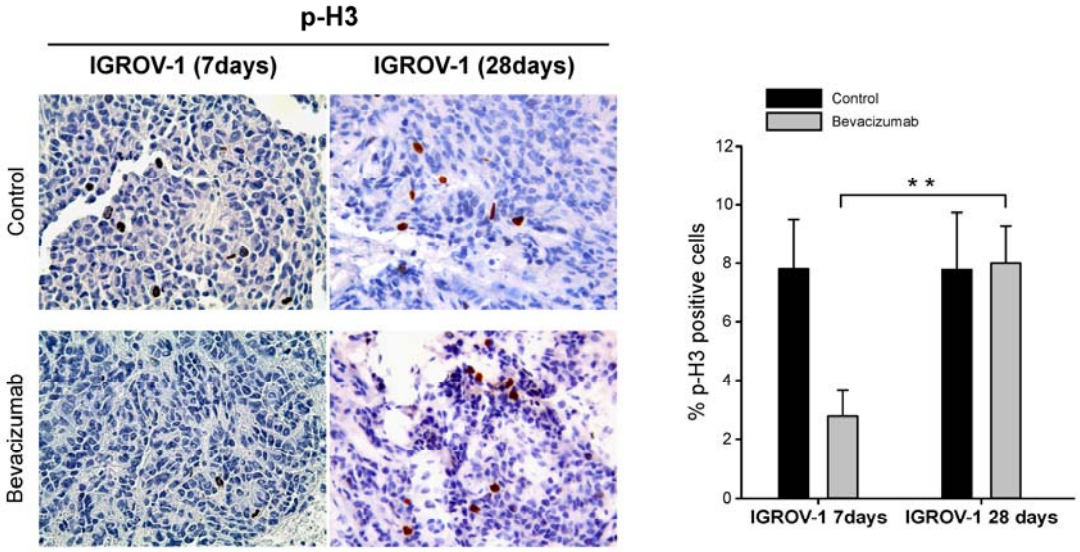

Suppl. Fig. 5

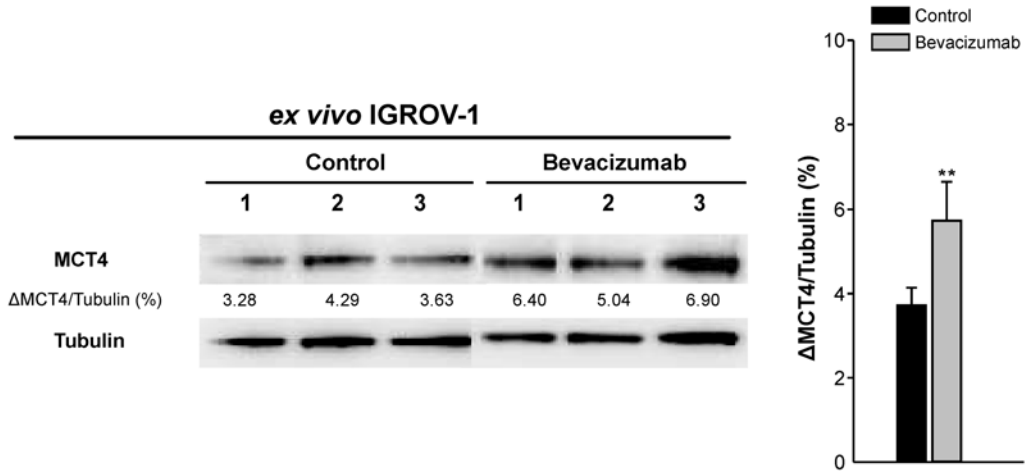

Suppl. Fig. 6

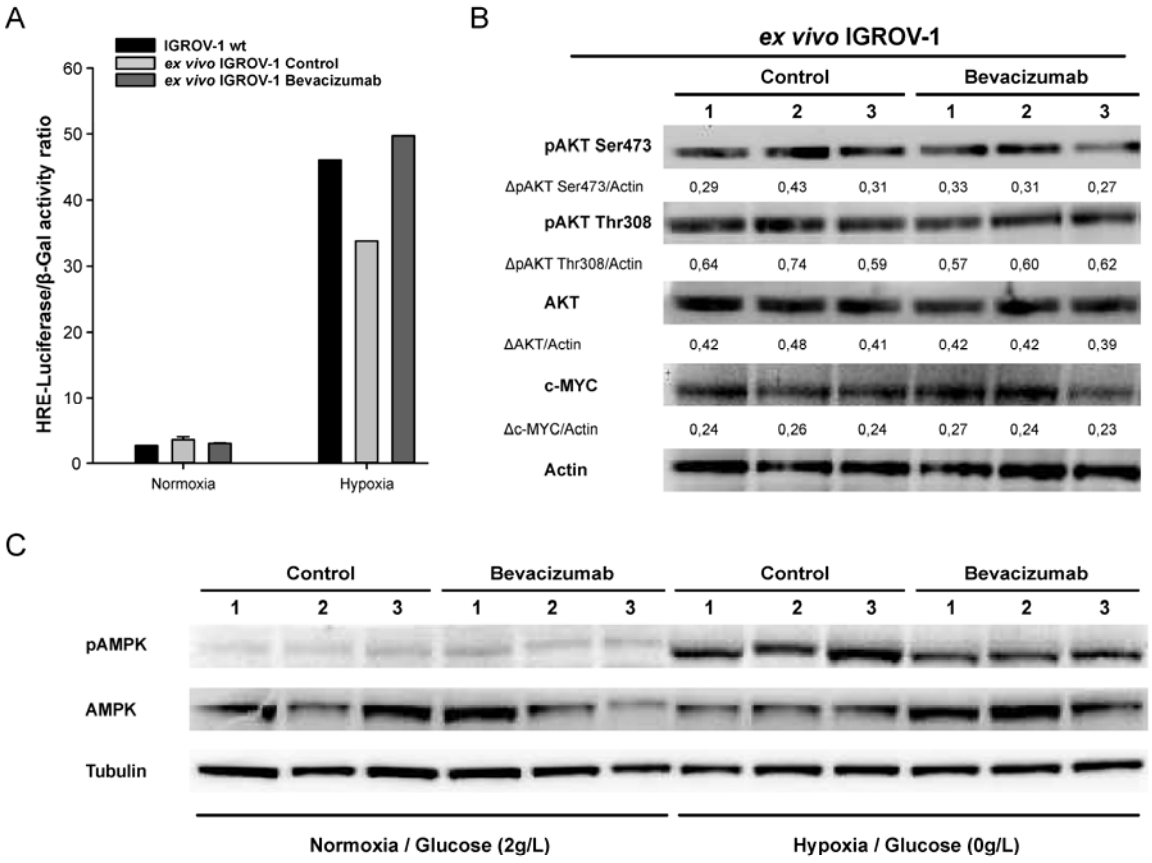
A
IGROV-1 wt
ex vivo IGROV-1 Control
ex vivo IGROV-1 Bevacizumab
HRE-Luciferase/β-Gal activity ratio
60
50
40
30
20
10
0
Normoxia
Hypoxia
B
ex vivo IGROV-1
Control
Bevacizumab
1 2 3 1 2 3
pAKT Ser473
ΔpAKT Ser473/Actin 0,29 0,43 0,31 0,33 0,31 0,27
pAKT Thr308
ΔpAKT Thr308/Actin 0,64 0,74 0,59 0,57 0,60 0,62
AKT
ΔAKT/Actin 0,42 0,48 0,41 0,42 0,42 0,39
c-MYC
Δc-MYC/Actin 0,24 0,26 0,24 0,27 0,24 0,23
Actin
C
Control
Bevacizumab
Control
Bevacizumab
1 2 3 1 2 3 1 2 3 1 2 3
pAMPK
AMPK
Tubulin
Normoxia / Glucose (2g/L)
Hypoxia / Glucose (0g/L)

Suppl. Fig. 7

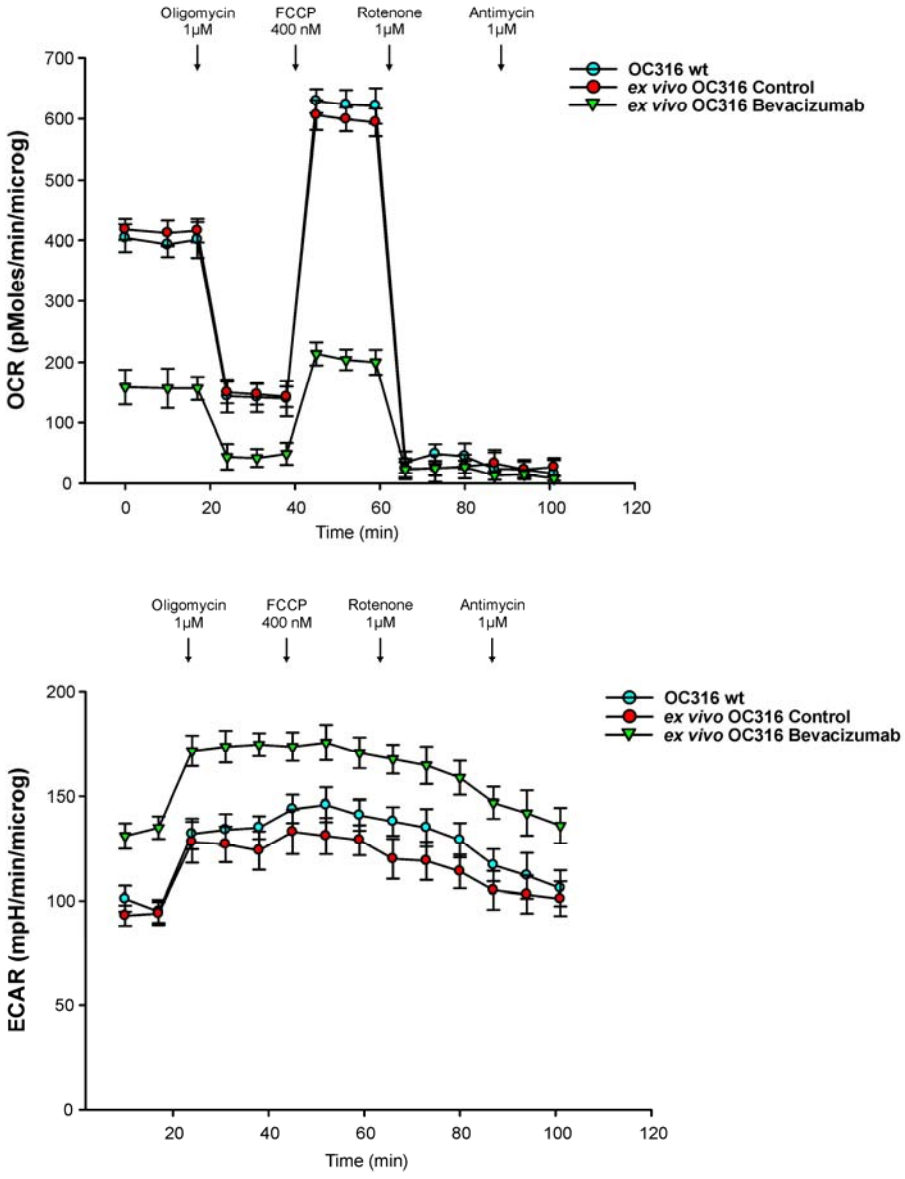
Oligomycin 1µM
FCCP 400 nM
Rotenone 1µM
Antimycin 1µM
OCR (pMoles/min/microg)
Time (min)
OC316 wt
ex vivo OC316 Control
ex vivo OC316 Bevacizumab
ECAR (mpH/min/microg)

Suppl. Fig. 8

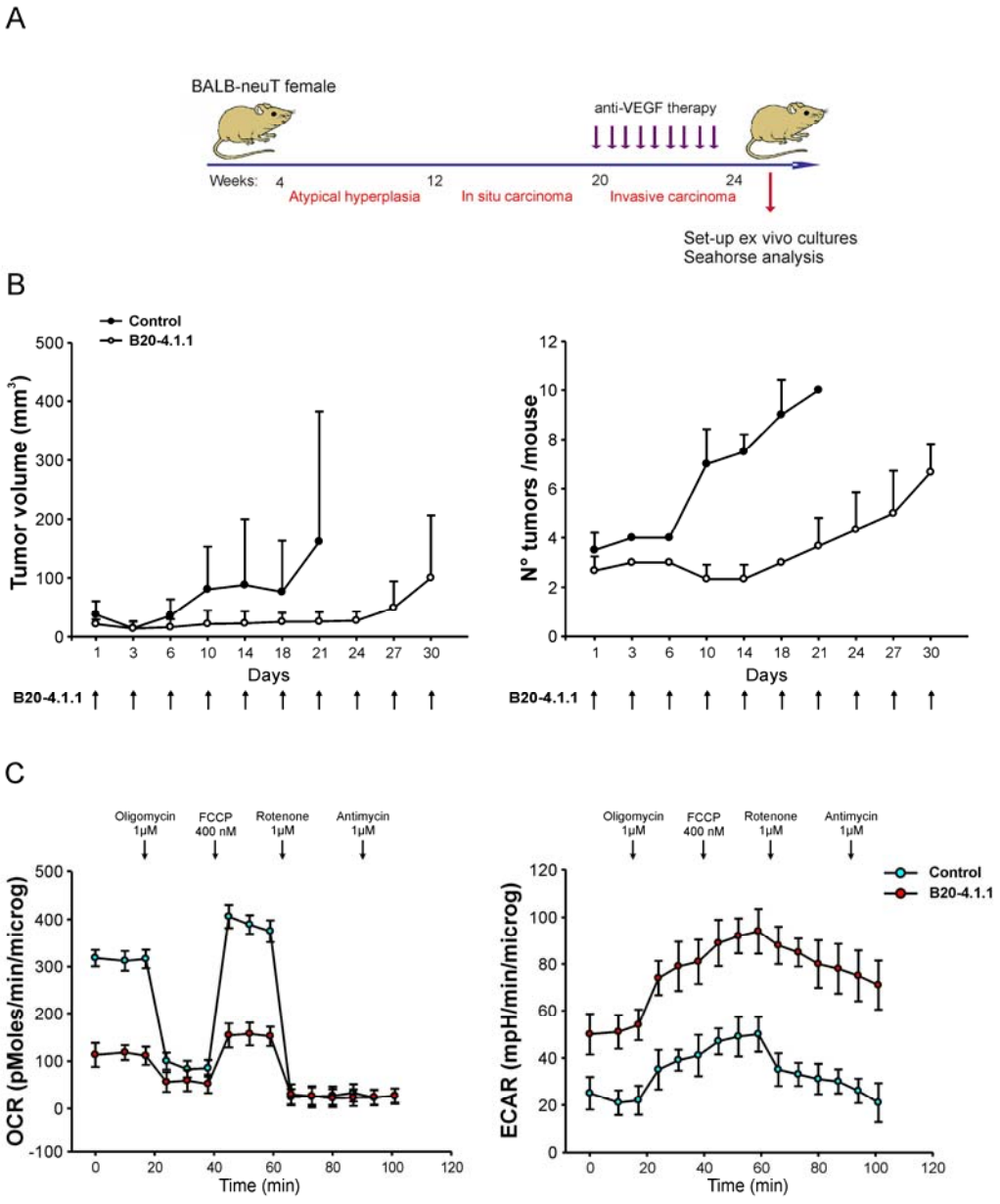
A
BALB-neuT female
anti-VEGF therapy
Weeks: 4
12
20
24
Atypical hyperplasia
In situ carcinoma
Invasive carcinoma
Set-up ex vivo cultures
Seahorse analysis
B
Control
B20-4.1.1
Tumor volume (mm3)
Days
B20-4.1.1
N° tumors /mouse
Days
B20-4.1.1
C
Oligomycin 1µM
FCCP 400 nM
Rotenone 1µM
Antimycin 1µM
OCR (pMoles/min/microg)
Time (min)
ECAR (mpH/min/microg)
Time (min)
Control
B20-4.1.1

Suppl. Fig. 9

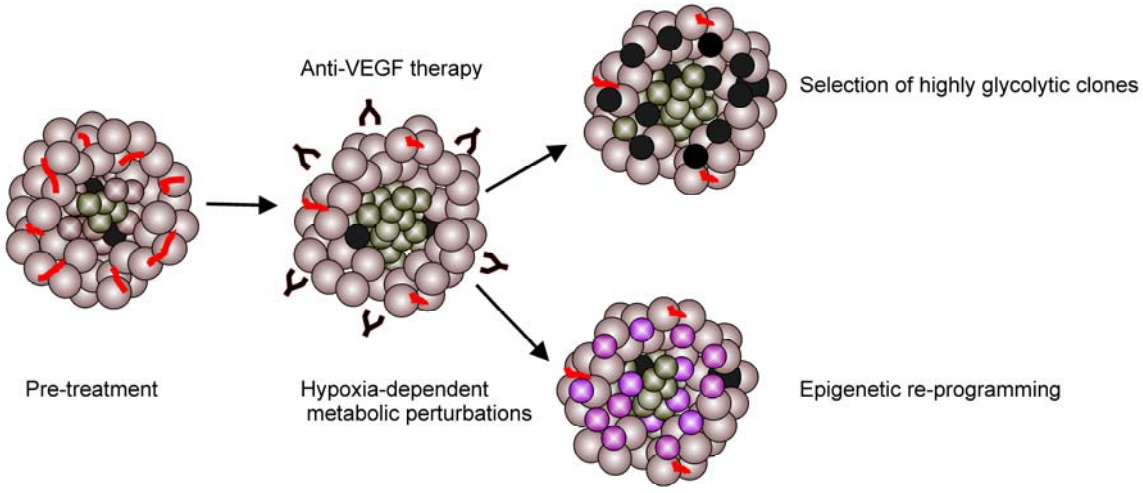

Reversible metabolic changes **Stable metabolic changes**

SUPPLEMENTARY FIGURE LEGENDS

Suppl. Figure 1. Characterization of cancer cell lines with different metabolic features.

A: Glucose consumption and lactate production *in vitro* is higher in MCF7 compared with SKOV3 cells. Cells were plated in P6 wells at 3.0 x 10^5 cells/well, incubated for 72 h *in vitro* under normoxic conditions and metabolic parameters quantified by an automatic analyser. Columns show mean ± SD values of three independent experiments, * $P< 0.05$, t-test compared to SKOV-3. The panel shows also glucose consumption and lactate production in OC316 and IGROV-1 cells, representative of highly and poorly glycolytic tumor cell lines, respectively.

B: Measurements of apoptosis by Annexin V staining of MCF7 and SKOV3 cells maintained under glucose starvation and hypoxia (0.5% pO_2) for 72 h or after treatment with the glycolysis inhibitor 2-DG (6g/L). Columns report the mean values ± SD of three independent experiments. * $P< 0.05$, t-test compared to SKOV-3.

Suppl. Figure 2. Anti-VEGF therapy reduces vascularization and increases necrosis in tumor xenografts.

A: Histological analysis shows larger necrotic areas in anti-VEGF-treated s.c. tumors compared with controls. Tumor samples were collected after 4 weeks of anti-VEGF therapy. Representative images (original magnification: x25) are shown. The continuous line marks the boards of necrotic tissue. Columns indicate quantitative analysis of necrotic areas in *n*=5 different tumors for each group, * $P< 0.05$, ** $P< 0.01$, t-test. *Right panel*: columns show tumor volume at sacrifice (mean ± SD values).

B: Vascularization of tumors by staining with anti-CD31 mAb and calculation of microvessel density (MVD). Representative images (original magnification: x200) are shown. Columns show mean ± SD values (n=5-10 fields for tumor; *n*=6 tumors for group), * $P< 0.05$, ** $P< 0.01$, t-test.

Suppl. Figure 3. AMPKα1/α2 silencing up-regulates glycolysis and renders tumors less responsive to anti-VEGF therapy.

A: Transduction of IGROV-1 cells with lentiviral vectors encoding two different shRNA targeting AMPKα1 and AMPKα2 modulates AMPKα1/α2 mRNA (*left*) and protein (*right*) expression levels, compared to controls (shRNA). Columns show AMPKα1 and AMPKα2 transcript (mean ± SD; 3 independent experiments). For Western blot analysis, cell lysates were obtained after 24 h cultivation of IGROV-1 cells under standard conditions (+) or glucose starvation (-).

B: Measurement of glucose consumption and lactate production. Cells were plated in P6 wells at 3.0×10^5 cells/well, incubated for 72 h *in vitro* under normoxic conditions and metabolic parameters quantified by an automatic analyzer. Mean ± SD of three experiments is shown. * $P < 0.05$, t-test.

C: Apoptosis by Annexin V staining of IGROV-1 cells bearing reduced AMPKα1/α2 levels compared to shRNA control under glucose starvation. Experiments were performed either under normoxic or hypoxic (0.5% pO_2) conditions. Columns report the mean values ± SD of 3 independent experiments. * $P < 0.05$, *** $P < 0.001$, t-test.

D: Kinetics of tumor development in SCID mice s.c. injected with IGROV-1 shRNA (*left panel*) and IGROV-1 shAMPKα1/α2 (*right panel*) tumor cells and effects of multiple injections of the anti-VEGF mAb bevacizumab (arrows, 100 µg/dose, administered every 2-3 days) on tumor size compared to the size of controls (*n*=6 mice for group). * $P< 0.05$, t-test.

Suppl. Figure 4. Effects of anti-VEGF therapy on tumor cell proliferation.

Measurement of proliferation in tumors by phospho-Histone3 (p-H3) IHC analysis. Staining was performed in tumor samples obtained at either 7 or 28 days after anti-VEGF treatment. Left panel show representative pictures of p-H3 reactivity in IGROV-1 xenografts. Right panel reports quantitative analysis of $p\text{-}H3^+$ cells in tumor samples (*n*=5-10 fields for tumor, *n*=5 tumors for group). **, P< 0.01, t-test.

Suppl. Figure 5. Expression MCT4 protein in *ex vivo* cultures of IGROV-1 tumors.

Western blot analysis of MCT4 levels in *ex vivo* cultures of IGROV-1 tumors. Tubulin was used as loading control. *Left panel:* Three representative tumors per group are shown. *Right panel:* Columns report the mean values ± SD of MCT4/Tubulin in all samples analyzed (n=5 *ex-vivo* IGROV-1 Bevacizumab and n=4 Control samples). **, P<0.01, t-test.

Suppl. Figure 6. Analysis of HIF-1α activity and expression levels of pAKT, c-MYC and pAMPK in *ex vivo* cultures of IGROV-1 tumors.

A: Analysis of HIF-1α activity in *ex vivo* cultures of IGROV-1 tumors. Tumor cells were lipofected with either an HRE-luciferase plasmid or an HREmut-luciferase plasmid (bearing a mutated HRE sequence) and a β-galactosidase encoding plasmid. Twenty-four hours later HIF-1α activity was measured by a luciferase reporter assay and normalized to β-galactosidase activity. The values obtained were normalized to luciferase/β-galactosidase activity of the matched HREmut-luciferase transfectants. The bars represent mean values ± SD of three different replicates. One experimental replicate maintained under hypoxic conditions (0.5% pO_2 for 24 h) was included as assay control.

B-C: Western blot analysis of pAKT, AKT, c-MYC, pAMPK, and AMPK levels in *ex vivo* cultures of IGROV-1 tumors. Actin and tubulin were used as loading controls. Three representative tumors per group were analysed. To activate AMPK, tumor cells were cultivated for 24 h under hypoxic conditions (0.5% pO_2) and glucose starvation.

Suppl. Figure 7. Bio-energetic analysis of *ex vivo* cultures of OC316 tumors resistant to anti-VEGF therapy.

Representative OCR and ECAR traces obtained from OC316 cells grown *in vitro* or obtained from mouse xenografts untreated (Control, average volume at sacrifice = 293,14 ± 191,21 mm^3) or treated for 2 weeks with anti-VEGF mAb (Bevacizumab, average volume at sacrifice = 165,30 ± 101,37 mm^3). Subsequent

additions of the ATP synthase inhibitor oligomycin, of the uncoupler FCCP, of the ETC complex I inhibitor rotenone and of the respiratory complex III inhibitor antimycin A were carried out. Data are mean ± SD values of n=10 replicates normalized to protein content. The experiment was repeated in n=5 independent *ex vivo* cultures per group with similar results.

Suppl. Figure 8. Selection of highly glycolytic cells in BALB-neuT transgenic mouse model following anti-VEGF therapy.

A: Time course of mammary tumor development in BALB-neuT mice and schedule of anti-VEGF therapy.

B: Effects of multiple injections of the anti-VEGF mAb B20-4.1.1 (arrows, 100 µg/dose, administered every 2-3 days) on tumor size (*left panel*) and on number of tumors per mouse (*right panel*) in BALB-neuT transgenic mice.

C: Representative OCR and ECAR traces of mammary tumors cells obtained from 21 week-old untreated BALB-neuT mice (Control) or treated for 4 weeks with anti-VEGF mAb (B20-4.1.1). Subsequent additions of the ATP synthase inhibitor oligomycin, of the uncoupler FCCP, of the ETC complex I inhibitor rotenone and of the respiratory complex III inhibitor antimycin A were carried out. Data are mean ± SD values of n=10 replicates normalized to protein content. Metabolic flux analysis was performed in n=5 independent *ex vivo* cultures per group with similar results.

Suppl. Figure 9. Working hypothesis: Evolutionary dynamics of tumor metabolism.

Following treatment of established tumors with an antiangiogenic drug (Y) hypoxia is increased, leading to HIF-1α-dependent up-regulation of glycolysis. Highly glycolytic tumor cells (green circles) will be mostly found in hypoxic areas, such as around necrotic areas. This initial modulation of tumor metabolism could possibly be reverted upon return to normoxic conditions. In parallel, antiangiogenic treatment could either drive selection of pre-existing highly glycolytic tumor cells (black circles) or lead to stable epigenetic

reprogramming of tumor metabolism (purple circles). In this case, highly glycolytic tumor cells will be found also distant from hypoxic/necrotic areas and tumors will bear both reversible and stable metabolic changes.

SUPPLEMENTARY DATA

MATERIALS AND METHODS

Table S1: primer sequences

Gene name	Forward	Reverse
GLUT-1	5'-GATGATGCGGGAGAAGAAGG-3'	5'-AAGACAGCGTTGATGCCAGAC-3'
GLUT-3	5'-CCCAGATCTTTGGTCTGGAA-3'	5'-AAGGGCTGCACTTTGTAGGA-3'
HKII	5'-GAAGATGCTGCCCACCTTTG-3'	5'-CACCCAAAGCACACGGAAGT-3'
PFK	5'-ACTGACGCCTGTCGCTTATG-3'	5'-GAGCGGGTTAGGTCCCTTCT-3'
GAPDH	5'-GAAGGTGAAGGTCGGAGT-3'	5'-CATGGGTGGAATCATATTGGAA-3'
PK	5'-AGAACATCCTGTGGCTGGAC-3'	5'-ACCTTTCTGCTTCACCTGGA-3'
LDH-A	5'-GATTCAGCCCGATTCCGTTAC-3'	5' ACTCCATACAGGCACACTGG-3'
MCT-1	5'-GTGGCTCAGCTCCGTATTGT-3'	5'-AGGACAGGACAGCATTCCAC-3'
MCT-4	5'-GTTGGGTTTGGCACTCAACT-3'	5'-GAAGACAGGGCTACCTGCTG-3'
AMPKα1	5'-GGAGCCTTGATGTGGTAGGA-3'	5'-GTTTCATCCAGCCTTCCATTC-3'
AMPKα2	5'-ACCAGCTTGCAGTGGCTTAT-3'	5'-CAGTGCATCCAATGGACATC-3'
β2micro	5'-TGCTGTCTCCATGTTTGATGTATCT-3'	5'-TCTCTGCTCCCCACCTCTAAGT-3'

SUPPLEMENTARY MATERIALS AND METHODS

Annexin-V apoptosis assay. Cells were incubated with Annexin V-FITC in Hepes buffer containing propidium iodide (PI), using the Annexin-V Fluos Staining Kit (Roche Diagnostics, Mannheim, Germany). Labelled cells were analysed by an EPICS-XL cytofluorimeter using Expo32 software (Beckman Coulter, Fullerton, CA).

Evaluation of microvessel density by immunofluorescence analysis. Tumor vessels were labelled with rat anti-CD31 mAb (1:50 dilution; cat. 550274; BD Pharmingen, Franklin Lakes, NJ) followed by staining with a goat anti-rat 546 secondary antibody (Invitrogen, Milan, Italy) and quantification of microvessel density as detailed elsewhere (1). Nuclei were stained with TOPRO-3 (Invitrogen).

Lentiviral vector-mediated transduction of shRNA in ovarian cancer cells. The lentiviral plasmids containing AMPKα2 shRNA expression cassette or AMPKα1 shRNA expression cassette or an unrelevant shRNA sequence were purchased from Sigma-Aldrich. The lentiviral vectors were produced as previously described (2). Cells expressing the shRNA were selected in puromycin-containing medium for 10-14 days prior to subsequent analysis.

Histology and immunohistochemistry. Quantification of necrosis was carried out by calculating the percentage of the necrotic area in the entire tumor section by using a light microscope equipped with digital camera and MODEL software (Leica Microsystems, Wetzlar, Germany). For immunohistochemical analysis, 5 μm-thick paraffin-embedded tumor sections were re-hydrated and then antigen retrieval was performed by incubation with citrate buffer 0.01M pH 6.0 at 95°C for 20 min. To evaluate proliferation and glycolytic activity, after saturation with 5% pre-immune serum, slides were incubated with rabbit anti-PH3 (#9701, Cell Signaling, Beverly, MA), rabbit anti-MCT4 (H-90) (sc-50329, Santa Cruz Biotechnology, Santa Cruz, CA) or rabbit anti-MCT1 (ab85021, Abcam, Cambridge Science Park, UK) Abs, respectively, according to the manufacturer's instructions. Specificity of the anti-MCT4 antibody - used by Whitaker-Menezes *et al*. in a previous paper (3) - was checked by silencing experiments in OC316 cells with MCT4-specific shRNA

(data not shown). Slides were subsequently washed and incubated with the appropriate secondary Ab. Immunostaining was performed using the avidin-biotin-peroxidase complex technique (Vectastain ABC kit, Vector Labs, Burlingame, CA) and 3-3' diaminobenzidine (DAB kit, Dako) was used as chromogen substrate. Finally, tumor sections were counterstained with Mayer's hematoxylin. Specificity of each staining procedure was confirmed by replacing the primary Ab with PBS. Immuno-reactivity was scored semi-quantitatively for both the intensity and the proportion of cells staining: intensity was given scores 0-3 (no staining = 0; light staining = 1; moderate staining = 2; strong staining = 3) and proportion was given scores 1-6 (0-4% = 1; 5-20% = 2; 21-40% = 3; 41-60% = 4; 61-80% = 5; 81-100% = 6). The two scores were multiplied to obtain the final result of 0-18. Biomarkers scoring was performed by an experienced pathologist (G.E.) blinded to the identity of the samples at a magnification of x100, based on the Quick Score Method (4). Analysis of clinical samples was approved by the institutional review board of Istituto Oncologico Veneto: additional clinical data are reported in detail elsewhere (4).

Positron emission tomography (PET) studies. [^{18}F]FLT and [^{18}F]FAZA were prepared as previously described with minor modifications and injected with a radiochemical purity greater than 99 % (5, 6). For PET studies, animals (n=20 for each cell line) were evaluated on consecutive days with both radioligands at baseline when tumor reached a volume of approximately 90-100 mm^3(day 0), randomly assigned to bevacizumab (n=10 for each cell group) or saline treatment and then reevaluated with PET at 7 days and 28 days after the beginning of treatment. [^{18}F]FLT PET studies were performed as follows: animals were injected in a tail vein with 4.28 ± 0.24 MBq of the tracer and images acquired at 60 minutes after tracer injection for 30 minutes. For [^{18}F]FAZA PET mice were injected i.v. with 5.71 ± 0.37 MBq and 15 minutes PET scans performed 120 minutes later. During acquisitions animals were maintained under slight gas anesthesia (isoflurane 2%). PET studies were acquired in three-dimensional mode and all images were reconstructed by using the EM (Expectation Maximization) algorithm. Data were corrected for the physical decay of fluorine 18 (t1/2: 109.8 minutes) and transformed in absolute radioactivity concentration values (MBq/gr) after calibration of the tomography using a standard phantom and considering tissue density equal to that

of water. Quantification analyses were performed using PMOD 2.7 software. For each animal maximal tumor to background ratios (Tmax/B) and volume of radioactivity uptake (Volmetab) were measured. To this aim, PET images were thresholded as previously validated and described by Krak et al. to create masks for the automatic extraction of the volume of tracer distribution (7, 8). First using Region of Interest (ROI), we calculated maximum radioligands concentration in tumor (MBq/g) (upper threshold value) and mean radioligands distribution in background (thorax muscle, MBq/g) (background value). Then lower threshold was calculated as the halfway value between upper threshold value and background value. This method allowed to automatically extract the metabolic tumor volume (cm^3) and the maximum and mean uptake of the tumor. Standardized Uptake Value (SUV) was calculated according to the formula: SUV = tumor concentration activity [MBq/g] / (injected activity [MBq] / animal weight [g]). To reduce variability in radioactivity concentration values, tracer uptake in tumor SUVs were normalized to the corresponding SUVmean levels of the background regions and indicated as tumor to background ratios (T/B values). The same procedure was used both for [^{18}F]FLT and for [^{18}F]FAZA. Volume changes measured at calliper and with [^{18}F]FLT and [^{18}F]FAZA between treatment and time were evaluated using two-way repeated measure ANOVA (factors treatment and time) followed by Bonferroni post-hoc test for multiple comparisons. Statistical significance was set at an alpha of 0.05 (two-sided).

Induced metabolic bioluminescence imaging (imBI). Freeze-clamped tumors were excised and cut into serial cryosections for structural hematoxylin and eosin (H&E) stainings and metabolic measurements. For quantitative measurement of ATP, lactate, glucose, and pyruvate the method of metabolic imaging with induced bioluminescence (imBI) was applied, as described before (9-11). In brief, reaction solutions containing specific enzymes that link the metabolite of interest to the luciferase of Photobacterium fischeri or Photinus pyralis, respectively, were applied to tumor cryosections. Light emission was induced in a temperature-stabilized reaction chamber, which was placed under a microscope (Axiophot, Zeiss, Oberkochen, Germany) connected to a 16bit CCD camera with an imaging photon counting system (iXon^{EM}+ DU-888, Andor Technology PLC, Belfast, Northern Ireland). The resulting images of the spatial distribution

of light intensities were calibrated using appropriate standards. Metabolite content was calculated in μmol/g tumor tissue. Images were displayed in colors coding for tissue concentration of metabolites in units of μmol/g. Computerized image analysis allowed for separate data assessment in selected histological areas of xenotransplanted tumors, e. g., vital tumor regions. Five tumors of IGROV-1 Control and IGROV-1 Bevacizumab, respectively, were analyzed using three sections from each tumor (N = 5; n = 15). All metabolite concentrations shown here were acquired exclusively from vital tumor regions. For further methodological details and representative calibration curves see (9, 10, 12, 13).

Reporter gene assay. IGROV-1 cells were transiently co-transfected using lipofectamine 2000 (Invitrogen) with a HIF-1α-responsive luciferase reporter construct kindly provided by Dr. Celeste M. Simon (Abramson Cancer Research Institute, Philadelphia, PA) - carrying the luciferase reporter gene under the control of a promoter containing HRE sequences (HRE-luciferase) - or a plasmid bearing a mutated HRE sequence (HREmut-luciferase). A plasmid encoding β-galactosidase under the control of the human CMV promoter was used to normalize transfection efficiency. Cell lysates were harvested 24 h post-transfection and luciferase and β-galactosidase assays were carried out using BriteLite Plus (Perkin-Elmer, Waltham, Massachusetts) and Tropix® Galacto-Light™ (Applied Biosystems, Foster City, CA), respectively, on a plate luminometer (Perkin-Elmer).

Western Immunoblotting. For Western blot analyses, cells from *ex vivo* cultures of IGROV-1 tumors, both from control and Bevacizumab treated cultures, were lysed at 4°C in a buffer composed by 140 mM NaCl, 20 mM Tris-HCl pH 7.4, 5 mM EDTA, 10% glycerol, 1% Triton X-100, in the presence of phosphatase and protease inhibitors (Sigma). Lysates were then cleared with a centrifugation at 13000*g* for 30min at 4°C, and proteins were quantified using a BCA Protein Assay Kit (Thermo Scientific-Pierce). Proteins extracted from total cell lysates were then boiled for 5 min in Laemmli sample buffer, separated in reducing conditions on SDS-polyacrylamide gels and transferred onto Hybond-C Extra membranes (Amersham-Pharmacia, Little Chalfont, UK) following standard methods. Primary antibodies were incubated 16 h at 4°C and, then, the blots was hybridized with a 1:5000 diluted HRP-conjugated anti-mouse or anti-rabbit Ab for

1 h (Amersham-Pharmacia). Proteins were visualized by enhanced chemiluminescence (Millipore). Anti-tubulin Ab (1:4000, T5168) is from Sigma Aldrich. Anti-actin Ab (1:500, sc-1615) is from Santa Cruz Biotechnology (Santa Cruz, CA). Anti-pAMPK (1:1000, #2531), anti-AMPK (1:1000, #2532), anti-pACC (1:1000, #3661), anti-ACC (1:750, #3662) and anti-pAKT Ser473 (1:1000, #4051) Abs are from Cell Signaling (Beverly, MA). Anti-pAKT Thr308 (1:1000, sc-16646-R), anti-AKT1/2 (1:500, sc-8312) and anti-MCT4 (1:1000, sc-50329) Abs are from Santa Cruz Biotechnology. Anti-c-MYC Ab (1:500, OP10L) is from Oncogene Research Products (Millipore). Anti-Ndufs1 Ab (1:5000, ab157221) is from Abcam (Cambridge Science Park, UK).

Mitochondrial mass evaluation. N-acrydine orange (NAO 20 μM, Invitrogen), which binds to cardiolipin in mitochondrial membranes, was utilized to evaluate mitochondrial mass. Samples were analyzed on a FACS Canto II flow cytometer (Becton Dickinson, Franklin Lakes, NJ). Data acquisition and analysis were performed using FACSDiva software.

Cell tracing experiment. Cells from bevacizumab-treated tumors or control IGROV-1 tumors were transduced with a lentiviral vector expressing EGFP, mixed 1:1 with cells from control tumors and injected s.c. in SCID mice (n=5 per group). At 100 mm^3 of average tumor volume, mice were sacrified or treated with Bevacizumab according to the usual schedule for 28 days. The percentage of EGFP positive cells in tumors was measured by LSRII flow cytometer (Becton Dickinson) either before or after anti-VEGF therapy. Data analysis were performed using FlowJo software.

REFERENCES

1. Favaro E, Nardo G, Persano L, Masiero M, Moserle L, Zamarchi R, et al. Hypoxia inducible factor-1alpha inactivation unveils a link between tumor cell metabolism and hypoxia-induced cell death. *Am J Pathol* 2008;**173**:1186-201.

2. Indraccolo S, Tisato V, Tosello V, Habeler W, Esposito G, Moserle L, et al. Interferon-alpha gene therapy by lentiviral vectors contrasts ovarian cancer growth through angiogenesis inhibition. *Hum Gene Ther* 2005;**16**:957-70.

3. Whitaker-Menezes D, Martinez-Outschoorn UE, Lin Z, Ertel A, Flomenberg N, Witkiewicz AK, et al. Evidence for a stromal-epithelial "lactate shuttle" in human tumors: MCT4 is a marker of oxidative stress in cancer-associated fibroblasts. *Cell Cycle* 2011;**10**:1772-83.

4. Zulato E, Bergamo F, De Paoli A, Griguolo G, Esposito G, De Salvo GL, et al. Prognostic significance of AMPK activation in advanced stage colorectal cancer treated with chemotherapy plus bevacizumab. *Br J Cancer* 2014;**111**:25-32.

5. Martin SJ, Eisenbarth JA, Wagner-Utermann U, Mier W, Henze M, Pritzkow H, et al. A new precursor for the radiosynthesis of [18F]FLT. *Nucl Med Biol* 2002;**29**:263-73.

6. Reischl G, Ehrlichmann W, Bieg C, Solbach C, Kumar P, Wiebe LI, et al. Preparation of the hypoxia imaging PET tracer [18F]FAZA: reaction parameters and automation. *Appl Radiat Isot* 2005;**62**:897-901.

7. Krak NC, Boellaard R, Hoekstra OS, Twisk JW, Hoekstra CJ, Lammertsma AA. Effects of ROI definition and reconstruction method on quantitative outcome and applicability in a response monitoring trial. *Eur J Nucl Med Mol Imaging* 2005;**32**:294-301.

8. Brepoels L, Stroobants S, Vandenberghe P, Spaepen K, Dupont P, Nuyts J, et al. Effect of corticosteroids on 18F-FDG uptake in tumor lesions after chemotherapy. *J Nucl Med* 2007;**48**:390-7.

9. Mueller-Klieser W, Walenta S. Geographical mapping of metabolites in biological tissue with quantitative bioluminescence and single photon imaging. *Histochem J* 1993;**25**:407-20.

10. Sattler UG, Walenta S, Mueller-Klieser W. A bioluminescence technique for quantitative and structure-associated imaging of pyruvate. *Lab Invest* 2007;**87**:84-92.

11. Walenta S, Wetterling M, Lehrke M, Schwickert G, Sundfor K, Rofstad EK, et al. High lactate levels predict likelihood of metastases, tumor recurrence, and restricted patient survival in human cervical cancers. *Cancer Res* 2000;**60**:916-21.

12. Hirschhaeuser F, Sattler UG, Mueller-Klieser W. Lactate: a metabolic key player in cancer. *Cancer Res* 2011;**71**:6921-5.

13. Walenta S, Schroeder T, Mueller-Klieser W. Lactate in solid malignant tumors: potential basis of a metabolic classification in clinical oncology. *Curr Med Chem* 2004;**11**:2195-204.